Energy Surfaces of Ellipsoidal Billiards

Jan Wiersig and Peter H. Richter

Institut für Theoretische Physik and Institut für Dynamische Systeme, University of Bremen, Postfach 330 440, 28334 Bremen, Germany

Z. Naturforsch. **51 a,** 219–241 (1996); received March 14, 1996

Energy surfaces in the space of action variables are calculated and graphically presented for general triaxial ellipsoidal billiards. As was demonstrated by Jacobi in 1838, the system may be integrated in terms of hyperelliptic functions. The actual computation, however, has never been done. It is found that generic energy surfaces consist of seven pieces, representing topologically different types of invariant tori. The character of the corresponding motion is discussed. Frequencies, winding numbers, and the location of resonances are also determined. The results may serve as a basis for perturbation theory of slightly modified systems, and for semi-classical quantization.

1. Introduction

Hamiltonian systems with three degrees of freedom have recently attracted considerable attention. Even though the interest is primarily directed towards nonintegrable dynamics, it is important to have integrable limiting cases available as a reference. Ellipsoidal billiards are highly non-trivial examples of this kind. Their integrability was demonstrated in 1838 by Carl Gustav J. Jacobi [1] who solved the problem of geodesic motion on the surface of an ellipsoid in D dimensions; when one of its principal axes shrinks to zero length, this geodesic motion becomes equivalent to billiard motion in a $(D-1)$-dimensional ellipsoid. Jacobi achieved separation of variables by introducing elliptic coordinates, but he did not care to explore the various possible types of motion, nor did he determine action integrals I_i or energy surfaces in the form $H(I_1, \ldots, I_D) = E$. Yet, the essential aspects of an integrable system's dynamics are contained in this expression, such as types of motion, bifurcations of tori, fundamental frequencies and their resonances. These are the ingredients of perturbation theory and help understand the transition from regular to chaotic behavior when parameter changes drive the dynamics into nonintegrable regimes [2], [3]. The other important application of action variables is in the semiclassical approach to quantization which has produced spectacular results in the recent past [4].

Reprint requests to Prof. P. H. Richter,
E-mail: prichter@physik.uni-bremen.de.

Pyramid shaped energy surfaces in three-dimensional action space were first computed and graphically rendered for integrable cases of rigid body dynamics [5], [6]. Ellipsoidal billiards with rotational symmetry were treated by Richter et al. [7]. The present paper is a continuation of that work.

Elliptic coordinates (ξ, η, ζ) will be used as separating variables; their conjugate momenta are (p_ξ, p_η, p_ζ), and the corresponding actions (I_ξ, I_η, I_ζ),

$$I_s = \frac{1}{2\pi} \oint p_s \, \mathrm{d}s, \; s = \xi, \eta, \zeta \, . \tag{1}$$

The energy surface $H(I_\xi, I_\eta, I_\zeta) = E$ turns out to be an assembly of seven patches, as the definition of action-angle variables depends on the type of invariant tori. Each individual patch is a bounded surface representing a family of 3-tori. The tori undergo bifurcations along the boundary of a patch which corresponds to non-generic motion on critical 2-tori or separatrices; corner points of a patch represent critical 1-tori, i. e., periodic orbits, or special 2-tori. Critical 2-tori may be hyperbolic, elliptic or parabolic; for elliptic tori it is always possible to define the actions in such a way that one of them becomes zero; we shall use this possibility as a matter of principle. The stability of 1-tori derives from the two stability types of the edges to which they belong.

This paper is organized as follows. In Sect. 2 we define the dynamical system and discuss some relevant properties of elliptic coordinates. Section 3 contains the bifurcation diagram and describes the

0932-0784 / 96 / 0400-0219 $ 06.00

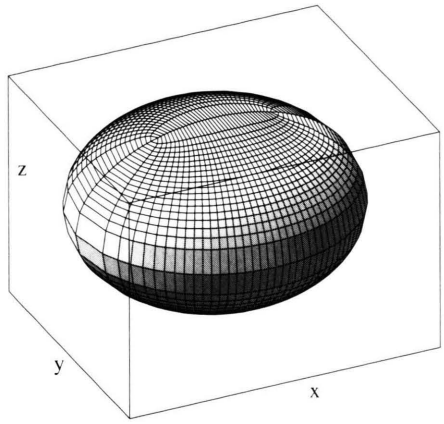

Fig. 1. Surface $\xi = 0.9$. The surfaces $\xi = \text{const}$ are confocal ellipsoids. For $\xi \to a$, they become flat elliptical discs in the (x, y)-plane, cf. Fig. 4; $\xi = 1$ is the billiard's boundary. The parameters are $(a, b) = (0.7, 0.3)$.

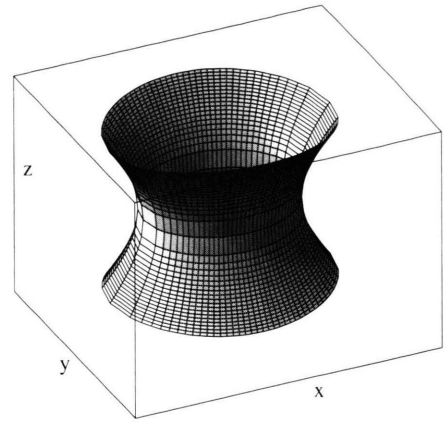

Fig. 2. Surface $\eta = 0.5$. The surfaces $\eta = \text{const}$ are confocal hyperboloids of one sheet. For $\eta \to a$, they are squeezed onto the (x, y)-plane where they leave an elliptical hole; for $\eta \to b$, they are pressed against the (x, z)-plane where they cover the area between the focal hyperbolas, cf. Figure 4. $(a, b) = (0.7, 0.3)$.

generic types of motion in terms of their caustics. In Sect. 4 we calculate action integrals I_s and present energy surfaces in action space, for different shapes of ellipsoids. Finally, in Sect. 5 we determine frequencies $\omega_s = \partial H/\partial I_s$, winding ratios, and the location of resonances on the energy surface.

2. The general triaxial ellipsoid

Consider the following boundary in $\mathbb{R}^3$,

$$x^2 + \frac{y^2}{1-b^2} + \frac{z^2}{1-a^2} = 1 \quad (0 \le b \le a < 1). \quad (2)$$

With a and b varying from 0 to 1 ($b \le a$), we have a two-parameter family of ellipsoids. Their major half axis is normalized to 1. The cases $b = 0$ (oblate ellipsoid), $b = a$ (prolate ellipsoid) and $b = a = 0$ (sphere) have already been treated in [7].

The Hamiltonian is separable in elliptical coordinates (ξ, η, ζ) as Jacobi [1] demonstrated in 1838[1]. Their relation to Cartesian (x, y, z)-coordinates is

$$(x, y, z) = \left(\frac{\xi\eta\zeta}{ab}, \frac{\sqrt{(\xi^2 - b^2)(\eta^2 - b^2)(b^2 - \zeta^2)}}{b\sqrt{a^2 - b^2}}, \frac{\sqrt{(\xi^2 - a^2)(a^2 - \eta^2)(a^2 - \zeta^2)}}{a\sqrt{a^2 - b^2}} \right), \quad (3)$$

[1]The (ξ, η, ζ) differ somewhat from his λ_i but have become standard among physicists, see [8] or [9].

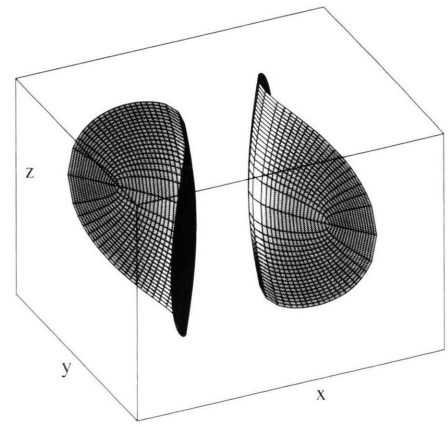

Fig. 3. Surface $\zeta = 0.2$. The surfaces $\zeta = \text{const}$ are confocal hyperboloids of two sheets. For $\zeta \to 0$, they approach the (y, z)-plane; for $\zeta \to b$, they cover the (x, z)-plane outside the focal hyperbolas, cf. Figure 4. $(a, b) = (0.7, 0.3)$.

which parametrizes the ellipsoid's octant of positive x, y, z by the rectangular (ξ, η, ζ)-box

$$0 \le \zeta \le b \le \eta \le a \le \xi \le 1; \quad (4)$$

the other parts of the ellipsoid are obtained by appropriate reflections.

Figures 1 to 4 illustrate how surfaces of constant ξ, η, or ζ foliate the ellipsoid $(a, b) = (0.7, 0.3)$. Surfaces $\xi = \text{const}$ are confocal ellipsoids (Figure 1). Their sections with the (x, y)-plane are ellipses with

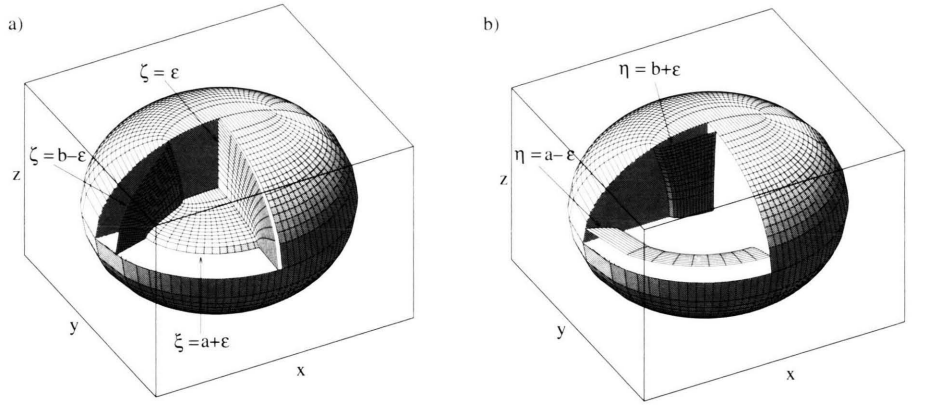

Fig. 4. Almost degenerate surfaces. The (x, y)-plane is covered by the combination of surfaces $\xi = a + \epsilon$ (a: flat ellipsoid) and $\eta = a - \epsilon$ (b: flat one-sheet hyperboloid); the (x, z)-plane is covered by the combination of surfaces $\eta = b + \epsilon$ (a: flat one-sheet hyperboloid) and $\zeta = b - \epsilon$ (b: flat two-sheet hyperboloid). $(a, b) = (0.7, 0.3)$.

foci at $(x, y) = (b, 0)$; their sections with the (x, z)-plane are ellipses with foci at $(x, z) = (a, 0)$; and their sections with the (y, z)-plane are ellipses with foci at $(y, z) = (\sqrt{a^2 - b^2}, 0)$. The innermost ellipsoid, $\xi = a$, degenerates to a double cover of the (x, y)-disk bounded by the focal ellipse

$$z = 0, \quad \frac{x^2}{a^2} + \frac{y^2}{a^2 - b^2} = 1, \tag{5}$$

see Fig. 4a; the outermost ellipsoid, $\xi = 1$, is the billiard's surface.

Surfaces $\eta = \text{const}$ are confocal hyperboloids of one sheet (Figure 2). Their sections with the (x, y)-plane are ellipses with foci at $(x, y) = (b, 0)$, continuing the intersections of family $\xi = \text{const}$; their sections with the (x, z)-plane are hyperbolas with foci at $(x, z) = (a, 0)$; and their sections with the (y, z)-plane are hyperbolas with foci at $(y, z) = (\sqrt{a^2 - b^2}, 0)$. There are two degenerate cases, see Figure 4: for $\eta = a$, the hyperboloid becomes a double cover of the elliptical annulus outside the focal ellipse in the (x, y)-plane; for $\eta = b$, it becomes a double cover of the (x, z)-region between the focal hyperbolas

$$y = 0, \quad \frac{x^2}{b^2} - \frac{z^2}{a^2 - b^2} = 1. \tag{6}$$

The intersection points of these hyperbolas with the ellipsoid $\xi = 1$ are

$$(x, y, z) = \left(\pm\frac{b}{a}, 0, \pm\frac{1}{a}\sqrt{(1 - a^2)(a^2 - b^2)} \right). \tag{7}$$

Surfaces $\zeta = \text{const}$ are confocal hyperboloids of two sheets (Figure 3). Their sections with the (x, y)-plane are hyperbolas with foci at $(x, y) = (b, 0)$; their sections with the (x, z)-plane are hyperbolas with foci at $(x, z) = (a, 0)$; they have no sections with the (y, z)-plane, but approach it in the limit $\zeta = 0$. The case $\zeta = b$ is degenerate in that it produces a double cover of the (x, z)-region outside the focal hyperbolas.

In the limit of oblate ellipsoids, $b \to 0$, the focal ellipse becomes the circle $x^2 + y^2 = a^2$, and the focal hyperbolas approach the z-axis. For prolate ellipsoids, $b \to a$, the focal ellipse becomes the line segment $-a \le x \le a$ along the x-axis while the focal hyperbolas approach the outer parts of the x-axis, $|x| \ge a$.

The Jacobian $\partial(x, y, z)/\partial(\xi, \eta, \zeta)$ diverges in the degenerate situations, i. e., on the (x, y)- and (x, z)-planes.

Figures 1 to 4 will help us determine the fundamental paths around the invariant tori for a given type of motion. This is important for the calculation of action integrals. In their configuration space projections, invariant tori have caustics which are made of pieces of constant elliptic coordinates.

It is straightforward to express the kinetic energy of free motion inside the ellipsoid, $T = \frac{1}{2}(\dot{x}^2 + \dot{y}^2 + \dot{z}^2)$, in

elliptical coordinates, and to determine the canonical momenta $p_s = \partial T/\partial \dot{s}$, $s = \xi, \eta, \zeta$. The Hamiltonian $H(\xi, \eta, \zeta, p_\xi, p_\eta, p_\zeta) = E$ turns out to be

$$\begin{aligned} 2H = & \frac{(\xi^2 - a^2)(\xi^2 - b^2)}{(\xi^2 - \eta^2)(\xi^2 - \zeta^2)} p_\xi^2 \\ & + \frac{(a^2 - \eta^2)(\eta^2 - b^2)}{(\xi^2 - \eta^2)(\eta^2 - \zeta^2)} p_\eta^2 \\ & + \frac{(a^2 - \zeta^2)(b^2 - \zeta^2)}{(\xi^2 - \zeta^2)(\eta^2 - \zeta^2)} p_\zeta^2. \end{aligned} \tag{8}$$

Reflection at the boundary $\xi = 1$ is simply described by

$$(\xi, \eta, \zeta, p_\xi, p_\eta, p_\zeta) \to (\xi, \eta, \zeta, -p_\xi, p_\eta, p_\zeta). \tag{9}$$

3. Bifurcation diagram and caustics

Separation of the Hamiltonian (8) is done in three steps. First, multiply by $\xi^2 - \eta^2$ and deduce

$$\begin{aligned} & 2E\xi^2 - \frac{(\xi^2 - a^2)(\xi^2 - b^2)}{\xi^2 - \zeta^2} p_\xi^2 \\ & \quad + \frac{(a^2 - \zeta^2)(b^2 - \zeta^2)}{\xi^2 - \zeta^2} p_\zeta^2 \\ = \; & 2E\eta^2 + \frac{(a^2 - \eta^2)(\eta^2 - b^2)}{\eta^2 - \zeta^2} p_\eta^2 \\ & \quad + \frac{(a^2 - \zeta^2)(b^2 - \zeta^2)}{\eta^2 - \zeta^2} p_\zeta^2. \end{aligned} \tag{10}$$

The first line is independent of (η, p_η), the second independent of (ξ, p_ξ), so both lines can be written as functions $K_3(\zeta, p_\zeta)$. Analogous statements are derived from multiplication of (8) by $\xi^2 - \zeta^2$ and by $\eta^2 - \zeta^2$, yielding functions $K_2(\eta, p_\eta)$ and $K_1(\xi, p_\xi)$.

In the second step, we combine the equations so obtained to find

$$\begin{aligned} 2E\xi^2 + K_1(\xi, p_\xi) &= 2E\eta^2 + K_2(\eta, p_\eta) \\ &= 2E\zeta^2 + K_3(\zeta, p_\zeta) \; = \; 4Ek, \end{aligned} \tag{11}$$

where k is a first separation constant.

In the third step, we use the explicit form of $K_1(\xi, p_\xi)$ in terms of $\xi, \zeta, p_\xi, p_\zeta$ to write the equation $2E\xi^2 + K_1(\xi, p_\xi) = 4Ek$ as

$$\begin{aligned} & 2E\xi^4 - (\xi^2 - a^2)(\xi^2 - b^2)p_\xi^2 - 2Ek\xi^2 = \\ & 2E\zeta^4 - (a^2 - \zeta^2)(b^2 - \zeta^2)p_\zeta^2 - 2Ek\zeta^2 =: 2El, \end{aligned} \tag{12}$$

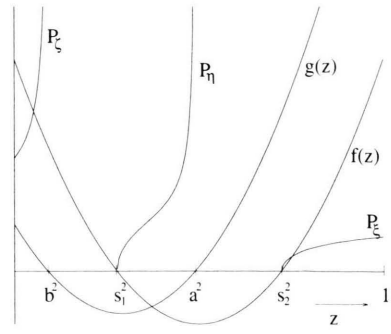

Fig. 5. Numerator $f(z)$ und denominator $g(z)$ of $p_s^2(s)$, as functions of $z = s^2$. In regions where $f/g \geq 0$, the positive branches of p_s are also drawn. The parameters are $(a, b) = (0.7, 0.3)$, and $(k, l) = (0.5, 0.2)$.

and similarly with the other two Equations (11). This identifies l as the second separation constant, and completes the procedure[2]. As a result, we have three independent equations

$$p_\xi^2 = 2E \frac{\xi^4 - 2k\xi^2 + l}{(\xi^2 - a^2)(\xi^2 - b^2)}, \tag{13}$$

$$p_\eta^2 = 2E \frac{-\eta^4 + 2k\eta^2 - l}{(a^2 - \eta^2)(\eta^2 - b^2)}, \tag{14}$$

$$p_\zeta^2 = 2E \frac{\zeta^4 - 2k\zeta^2 + l}{(a^2 - \zeta^2)(b^2 - \zeta^2)}, \tag{15}$$

and three constants of motion, with values E, k, and l. Hence, the Liouville-Arnol'd theorem [11] implies that the 5-dimensional energy shell is foliated by invariant 3-tori. Equations (13) to (15) describe the projections of these tori onto the (ξ, p_ξ), (η, p_η), and (ζ, p_ζ)-planes, respectively.

The energy constant E may be scaled away by measuring momenta p_s in units of $\sqrt{2E}$. This will be done in the following, hence the factor $2E$ will be omitted in (13)-(15). Note that these equations can be written as one, if (s, p_s) is taken for any of the three conjugate pairs of variables,

$$p_s^2 = \frac{s^4 - 2ks^2 + l}{(s^2 - a^2)(s^2 - b^2)} =: \frac{f(s^2)}{g(s^2)}, \tag{16}$$

and s chosen from the appropriate subinterval of

$$0 \leq s \leq 1. \tag{17}$$

[2] The separation of the Hamilton-Jacobi-equation as done in [10] is of course equivalent.

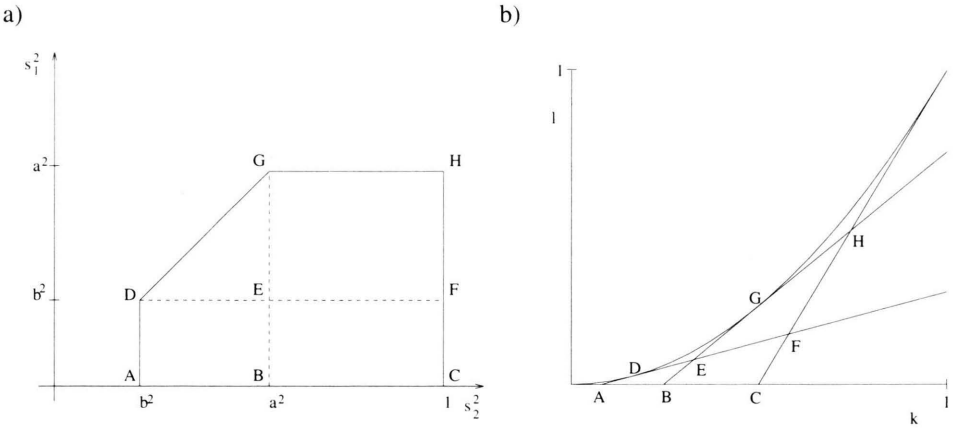

Fig. 6. Bifurcation diagrams of the ellipsoidal billiard. a) s_1^2 and s_2^2 as constants of motion. The allowed parameter range as defined by conditions (20) is divided into four regions by the lines $s_1^2 = b^2$ and $s_2^2 = a^2$; each region represents a distinct topological type of invariant 3-tori. b) Separation constants k and l as bifurcation parameters. – The relation between the two parameter sets is given in (19).

The functions $f(z)$ and $g(z)$ are polynomials of second degree in their arguments $z = s^2$; $g(z)$ has constant coefficients, $f(z)$ depends on the separation constants k and l. Figure 5 shows a typical graph.

The range of possible values (k, l) is determined by the following consideration. All momenta p_s must be real, so p_s^2 must be positive. Inspection of Fig. 5 shows that this requires $f(z)$ to be simultaneously positive somewhere in the intervals $[0, b^2]$, $[a^2, 1]$, and negative somewhere in $[b^2, a^2]$. The various possibilities are most conveniently discussed in terms of the real zeroes s_1^2, s_2^2, of $f(z)$,

$$p_s^2 = \frac{(s^2 - s_2^2)(s^2 - s_1^2)}{(s^2 - a^2)(s^2 - b^2)} \tag{18}$$

with

$$s_{1,2}^2 = k \mp \sqrt{k^2 - l}. \tag{19}$$

The conditions for all three p_s to assume real values are then

$$s_1 \leq s_2, \quad 0 \leq s_1 \leq a, \quad b \leq s_2 \leq 1. \tag{20}$$

The transformation (19) between parameters (k, l) and (s_1, s_2) is singular at $k^2 = l$ or $s_1 = s_2$.

Fig. 6 shows the physically allowed range of parameters, both in the (s_1^2, s_2^2)-plane of zeroes, and in the (k, l)-plane of separation constants. The corners D and G in Fig. 6a are tangencies in Fig. 6b, due to the singularity of the transformation (19).

The two lines $s_1 = b$ and $s_2 = a$ mark bifurcations in the topological type of invariant tori; they divide the allowed parameter space into four regions of different type of motion. The bifurcation at $s_1 = b$ involves the focal hyperbola (6). As long as $s_1 < b$, the values of ζ are confined to $\zeta \leq s_1 < b$, whereas η may assume the value b. Inspection of Fig. 4 shows that this means orbits cross the (x, z)-plane in the region *between* the focal hyperbolas. For $s_1 > b$, on the other hand, the opposite situation holds, and orbits cross the (x, z)-plane in the regions *outside* the focal hyperbolas. Physically speaking, this is a transition from oscillatory motion, back and forth through the hyperbolic disc $\eta = b$, to rotational ζ-motion around the z-axis. In the critical case $s_1 = b$, and only in this case, does the motion reach the (x, z)-plane on both sides of – and also in – the focal hyperbolas. In particular, motion in the (x, z)-plane that crosses the focal hyperbolas requires $\eta = \zeta = b$ and therefore $s_1 = b$.

The bifurcation at $s_2 = a$ involves the focal ellipse (5). As long as $s_2 < a$, the values of η are restricted to $\eta \leq s_2 < a$, whereas ξ may assume the value a. This means orbits cross the (x, y)-plane *inside* the focal ellipse, oscillating between top $(z > 0)$ and bottom $(z < 0)$ surfaces of the ellipsoid. For $s_2 > a$, on the other hand, η reaches the value a, and ξ stays away from it; this means orbits cross the (x, y)-plane

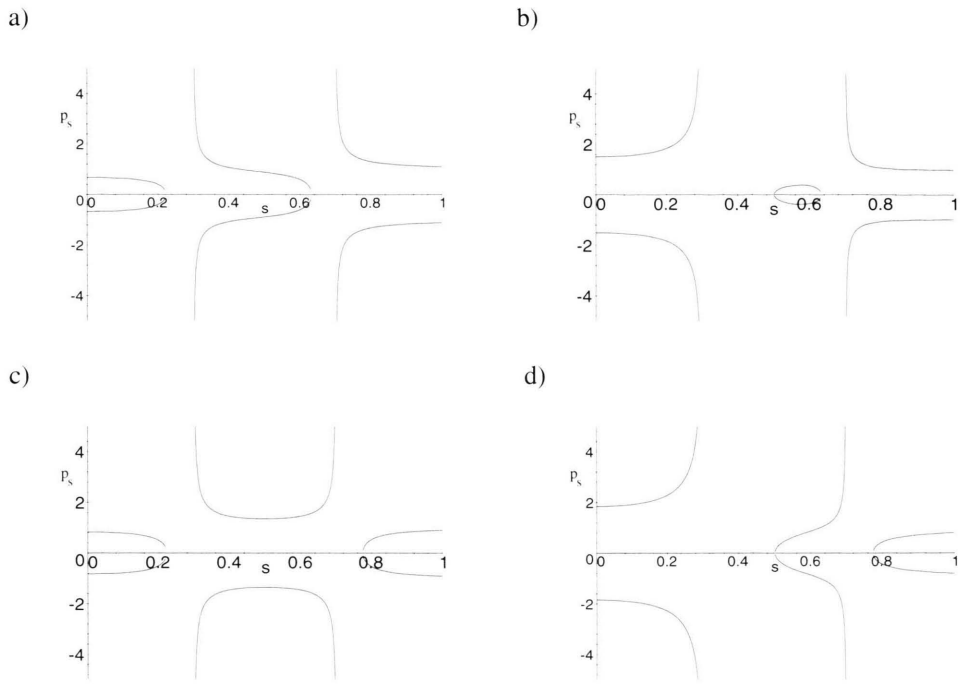

Fig. 7. Projection of the four types of invariant 3-tori onto the three planes of conjugate variables (s, p_s), s being ζ, η, ξ, respectively in the intervals $(0, b)$, (b, a), $(a, 1)$. The ellipsoid parameters are $(a, b) = (0.7, 0.3)$. a) $(s_1^2, s_2^2) = (0.05, 0.4)$. All three variables oscillate: ξ across the (x, y)-plane through the focal ellipse; η across the (x, z)-plane between the focal hyperbolas; ζ across the (y, z)-plane. b) $(s_1^2, s_2^2) = (0.25, 0.4)$. ξ behaves as in a); the η-oscillations do not reach singular values; ζ rotates around the z-axis. c) $(s_1^2, s_2^2) = (0.05, 0.6)$. ξ oscillates within a given coordinate sheet; η rotates around the x-axis; ζ oscillates as in a). d) $(s_1^2, s_2^2) = (0.25, 0.6)$. ξ behaves as in c); η-oscillates across the (x, y)-plane; ζ rotates around the z-axis.

through the elliptic ring *outside* the focal ellipse. The physical interpretation of this bifurcation depends on s_1. If the (x, z)-plane crossing is between the focal hyperbolas ($s_1 < b$), the transition opens the way for η-rotations around the x-axis. However, if orbits rotate already around the z-axis ($s_1 > b$), the transition merely reorganizes the ξ-oscillation, from passing through the focal ellipse to surrounding it. The critical case $s_2 = a$ corresponds to motion that either crosses the (x, y)-plane both inside and outside the focal ellipse, or is even confined to the (x, y)-plane and intersects the focal ellipse.

The special point $(s_1, s_2) = (b, a)$, corresponding to $(k, l) = (\frac{a^2+b^2}{2}, a^2b^2)$, is the only case where all three variables (ξ, η, ζ) simultaneously cover their entire ranges. As an intersection of separatrices, this point in parameter space indicates particularly complex behavior, including one-, two-, and three-dimensional motion: unstable linear motion along the x-axis; motion in the (x, y)-plane that passes through the foci at $(x, y) = (\pm b, 0)$; motion in the (x, z)-plane that passes through the foci at $(x, z) = (\pm a, 0)$; motion that passes through both focal lines and reaches every point in the ellipsoid.

Figures 7 and 8 illustrate the typical features of invariant 3-tori of the four types. Consider first the projections of tori onto the three planes of conjugate variables (s, p_s) in Figure 7. The s-interval is to be interpreted as ζ, η, and ξ in the subintervals $(0, b)$, (b, a), and $(a, 1)$, respectively; the corresponding momenta p_s are computed with (16). Whenever a variable s reaches the boundary of its interval, this means it has to be continued on another coordinate sheet (except at $\xi = 1$ where reflection $p_\xi \to -p_\xi$ takes place). In Fig. 7a this happens three times: when variable ξ reaches the value a, when η reaches the value b, and ζ the value 0. These instances are crossings of the Cartesian (x, y)-, (x, z)-, and (y, z)-planes, respectively. A full picture of this type of motion contains two sheets for each (s, p_s)-pair.

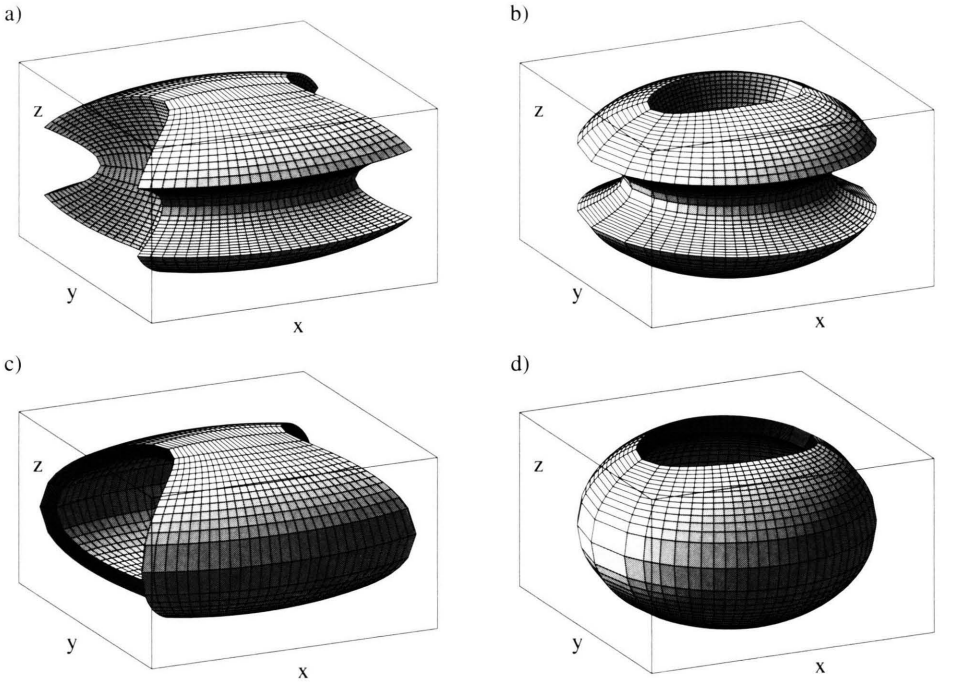

Fig. 8. Caustics of the four types of invariant 3-tori for the ellipsoid $(a, b) = (0.7, 0.3)$. a) Oscillations of the three variables ξ, η, ζ are across the (x, y)-, (x, z)-, and (y, z)-planes, respectively. b) Instead of oscillations across the (x, z)-plane, there are now rotations around the z-axis. c) Compared to a), the oscillations across the (x, y)-plane have turned into rotations about the x-axis. d) Oscillations in radial (ξ) and polar (η) directions, plus rotations around the z-axis.

Between Figs. 7a and b, a bifurcation at $s_1 = b$ has taken place. ξ remains unaffected, but η now oscillates within a single sheet whereas ζ changes its sheet at both ends of the interval $(0, b)$. This means ζ visits four sheets, on its rotation around the z-axis.

Between Figs. 7a and c, a bifurcation at $s_2 = a$ has taken place. ζ remains unaffected, ξ gets restricted to a single sheet, and η changes sheet at both ends, indicating rotational η-motion about the x-axis.

Finally, in Fig. 7d, both bifurcations have taken place, the result being that ξ is restricted to a single sheet, η visits two, and ζ four sheets; the rotational variable is ζ.

These observations are perhaps best illustrated in Fig. 8 where we show examples of caustics for the four types of tori. Caustics are the envelopes of motion in configuration space; they are very easily obtained by drawing the coordinate surfaces corresponding to the extreme values of ξ, η, and ζ that a given 3-torus attains. Billiard trajectories should be imagined to lie inside these figures, being normal to the outer surface $\xi = 1$, and tangential to all other surfaces. It is intuitively obvious from this representation that there are three oscillating degrees of freedom in Fig. 8a, and two oscillating plus one rotating degrees of freedom in the other three cases. The rotation is around the z-axis in Figs. 8b, d, and around the x-axis in Figure. 8c.

4. Calculation of actions and energy surfaces

Action integrals of Liouville-Arnol'd tori are canonical invariants of great physical importance[3]. When a system can be separated by choosing appropriate coordinates, it is straightforward to express the actions as closed-loop integrals. For ellipsoidal billiards, Jacobi's (ξ, η, ζ) and the corresponding momenta (p_ξ, p_η, p_ζ) provide three (s, p_s)-planes onto which the invariant 3-tori may be independently projected, each projection defining a closed integration

[3] According to an assertion by S. Chandrasekhar in the preface to K. Schwarzschild's Collected Papers [12] it was Schwarzschild who coined the term *action integrals* as we use it today, in his 1916 paper on quantization [13].

path for the three action integrals

$$I_\xi = \frac{1}{2\pi}\oint p_\xi \,\mathrm{d}\xi,$$
$$I_\eta = \frac{1}{2\pi}\oint p_\eta \,\mathrm{d}\eta, \qquad (21)$$
$$I_\zeta = \frac{1}{2\pi}\oint p_\zeta \,\mathrm{d}\zeta.$$

This is a very natural way to arrive at the actions, and will be followed here; we note only in passing that at times it may be advisable to take linear combinations of these integrals, with integer coefficients, corresponding to the group structure of fundamental paths on a torus.

Using s_1 and s_2 as convenient parameters to label the tori, all three action integrals have the general form, cf. (18),

$$I_s = \frac{1}{2\pi}\oint p_s \,\mathrm{d}s = \frac{n_s}{2\pi}\int_{s_-}^{s_+} \sqrt{\frac{(s^2-s_2^2)(s^2-s_1^2)}{(s^2-a^2)(s^2-b^2)}}\,\mathrm{d}s. \qquad (22)$$

The limits of integration $s_\pm$ and the integer numbers n_s depend on the given case and must be determined separately for each class, Fig. 5 and 7 serving as a guide. For example, a torus of the type shown in Fig. 7a has $(\zeta_-, \zeta_+) = (0, s_1)$, $(\eta_-, \eta_+) = (b, s_2)$, and $(\xi_-, \xi_+) = (a, 1)$; all three coordinates visit two sheets, hence all closed-loop integrals (21) are made of four equal pieces: $n_s = 4$ for $s = \zeta$, η, and ξ.

The number of tori for given (s_1, s_2) depends on whether or not there is rotational motion involved. Rotations come in two orientations, so every rotating coordinate contributes a factor 2 to the multiplicity m of tori. We saw in the preceding section that the elliptic billiard has never more than one rotation; in the example of Fig. 7a there is only oscillatory motion, so $m = 1$. The other three cases in Fig. 7 each have one rotating coordinate, so $m = 2$.

Table 1 assembles this kind of information for all possible integrals (22), first for the four generic types of motion, then for the degenerate cases along the boundary of the bifurcation diagram, Fig. 6a, and in the last seven entries, for the separatrix lines D-F and B-G. The criticality of tori along the boundary is expressed by the fact that one of the actions vanishes:

Table 1. Parameters for action integrals in various parts of the (s_1, s_2) bifurcation diagram. Underlined numbers n_ζ or n_η indicate rotational motion.

	s_1	s_2	m	n_ζ	n_η	n_ξ	ζ_-	ζ_+	η_-	η_+	ξ_-	ξ_+
ABED	$0 < s_1 < b$	$b < s_2 < a$	1	4	4	4	0	s_1	b	s_2	a	1
BCFE	$0 < s_1 < b$	$a < s_2 < 1$	2	4	$\underline{4}$	2	0	s_1	b	a	s_2	1
DEG	$b < s_1 < a$	$b < s_2 < a$	2	$\underline{4}$	2	4	0	b	s_1	s_2	a	1
EFHG	$b < s_1 < a$	$a < s_2 < 1$	2	$\underline{4}$	4	2	0	b	s_1	a	s_2	1
A	0	b	1	-	-	4	-	-	-	-	a	1
A-B	0	$b < s_2 < a$	1	-	4	4	-	-	b	s_2	a	1
B−	0	$a-$	1	-	4	4	-	-	b	a	a	1
B+	0	$a+$	2	-	$\underline{4}$	2	-	-	b	a	a	1
B-C	0	$a < s_2 < 1$	2	-	$\underline{4}$	2	-	-	b	a	s_2	1
C	0	1	2	-	$\underline{4}$	-	-	-	b	a	-	-
C-F	$0 < s_1 < b$	1	2	4	$\underline{4}$	-	0	s_1	b	a	-	-
F	b	1	2	$\underline{4}$	$\underline{4}$	-	0	b	b	a	-	-
F-H	$b < s_1 < a$	1	2	$\underline{4}$	4	-	0	b	s_1	a	-	-
H	a	1	2	$\underline{4}$	-	-	0	b	-	-	-	-
G-H	a	$a < s_2 < 1$	2	$\underline{4}$	-	2	0	b	-	-	s_2	1
G+	a	$a+$	2	$\underline{4}$	-	2	0	b	-	-	a	1
G−	a	$a-$	2	$\underline{4}$	-	4	0	b	-	-	a	1
D-G	$b < s_1 < a$	$s_2 = s_1$	2	$\underline{4}$	-	4	0	b	-	-	a	1
D+	$b+$	b	2	$\underline{4}$	-	4	0	b	-	-	a	1
D−	$b-$	b	1	4	-	4	0	b	-	-	a	1
A-D	$0 < s_1 < b$	b	1	4	-	4	0	s_1	-	-	a	1
(D-E)−	$b-$	$b < s_2 < a$	1	4	4	4	0	b	b	s_2	a	1
(D-E)+	$b+$	$b < s_2 < a$	2	$\underline{4}$	2	4	0	b	b	s_2	a	1
E-F	b	$a < s_2 < 1$	2	$\underline{4}$	$\underline{4}$	2	0	b	b	a	s_2	1
(B-E)−	$0 < s_1 < b$	$a-$	1	4	4	4	0	s_1	b	a	a	1
(B-E)+	$0 < s_1 < b$	$a+$	2	4	$\underline{4}$	2	0	s_1	b	a	a	1
(E-G)−	$b < s_1 < a$	$a-$	2	$\underline{4}$	2	4	0	b	s_1	a	a	1
(E-G)+	$b < s_1 < a$	$a+$	2	$\underline{4}$	4	2	0	b	s_1	a	a	1

I_ζ between A and C, I_ξ between C and H, I_η between A and H. Points A, C, and H represent tori where two actions are zero, i. e., periodic orbits. These are the linear oscillation along the z-axis (A), and two cases of sliding motion on the billiard's surface, following the smallest (C) and largest (H) circumference, respectively.

We remark here that for comparison (and for purposes of quantization) it is interesting to consider the symmetry reduced ellipsoidal billiard, where x, y, z are restricted to positive values, with elastic reflection at the three planes $x = 0$, $y = 0$, $z = 0$. Its actions are also given by (22), with parameters as in Table 1, except that all n_s are equal to 2, and all multiplicities $m = 1$.

The general integral (22) is hyperelliptic and must be evaluated by numerical methods. The only practical problem comes from the square-root singularities in the denominator. To solve it, we first substitute

$z = s^2$ and expand the integrand so that all integrals take the form

$$I_s = \frac{n_s}{4\pi} \int_{s_-^2}^{s_+^2} \frac{(z - s_2^2)(z - s_1^2)}{\sqrt{-\prod_{i=1}^{6}(z - z_i)}} \sqrt{1 - z}\, \mathrm{d}z, \quad (23)$$

where the six z_i are $\{0, b^2, a^2, s_1^2, s_2^2, 1\}$. In each particular case, the limits of integration s_-^2 and s_+^2 are two adjacent values of these z_i. To deal with the corresponding singularities, we substitute $z = s_-^2 \cos^2 t + s_+^2 \sin^2 t$, with t ranging from 0 to $\pi/2$, and obtain

$$I_s = \frac{n_s}{2\pi} \int_0^{\frac{\pi}{2}} \frac{(z(t) - s_2^2)(z(t) - s_1^2)}{\sqrt{\prod_{i=1}^{4}(z(t) - z_i')}} \sqrt{1 - z(t)}\, \mathrm{d}t, \quad (24)$$

where the four zeroes z_i' are the z_i without s_-^2 and s_+^2, and lie outside the interval of integration. The singularities have disappeared, and after a regularization (done by H.Dullin) standard integration algorithms may be applied, see [14].

The actions on boundaries and separatrices can be computed analytically for most cases. Except along the line C-H, the hyperelliptic integrals listed in Table 1 reduce to elliptic or even elementary integrals. Let us discuss typical examples. At point A we have $(s_1, s_2) = (0, b)$, hence $I_\eta = I_\zeta = 0$, and

$$\begin{aligned} I_\xi &= \frac{2}{\pi} \int_{a^2}^{1} \frac{s\, \mathrm{d}s}{\sqrt{s^2 - a^2}} \\ &= \frac{1}{\pi} \int_{a}^{1} \frac{\mathrm{d}t}{\sqrt{t - a^2}} \\ &= \frac{2}{\pi} \sqrt{1 - a^2}. \end{aligned} \quad (25)$$

Between A and B, we have $s_1 = 0$, hence $I_\zeta = 0$, but

$$\begin{aligned} I_\eta &= \frac{2}{\pi} \int_{b}^{s_2} \sqrt{\frac{s_2^2 - s^2}{(a^2 - s^2)(s^2 - b^2)}}\, s\, \mathrm{d}s \\ &= \frac{1}{\pi} \int_{b^2}^{s_2^2} \sqrt{\frac{s_2^2 - t}{(a^2 - t)(t - b^2)}}\, \mathrm{d}t \\ &= \frac{2}{\pi} \sqrt{a^2 - b^2} \left(\mathcal{E}(q) - (1 - q^2)\, \mathcal{K}(q) \right), \end{aligned} \quad (26)$$

where $\mathcal{K}(q)$ and $\mathcal{E}(q)$ are complete elliptic integrals of first and second kind, with modulus $q^2 = (s_2^2 - b^2)/(a^2 - b^2)$, and

Table 2. Action integrals $\frac{\pi}{2}(I_\zeta, I_\eta, I_\xi)$ for the four "corners" of point E.

E	$s_2 = a-$	$s_2 = a+$
$s_1 = b+$	$(b, \frac{a-b}{2}, 1-a)$	$(b, a-b, \frac{1-a}{2})$
$s_1 = b-$	$(b, a-b, 1-a)$	$(b, a-b, \frac{1-a}{2})$

Table 3. Action integrals $\frac{\pi}{2} I_\zeta$ for degenerate tori. I_ζ vanishes along the line A-C in the bifurcation diagram; it is hyperelliptic along the line C-F-H.

	$(\pi/2) I_\zeta$	q	$\sin\mu$
A-D	$a\left(\mathcal{E}(q) - (1-q^2)\mathcal{K}(q)\right)$	s_1/a	-
D	$a\left(\mathcal{E}(q) - (1-q^2)\mathcal{K}(q)\right)$	b/a	-
D-G	$a\left(\mathcal{E}(q) - (1-s_1^2/a^2)\mathcal{K}(q)\right)$	b/a	-
G	$a\,\mathcal{E}(q)$	b/a	-
G-H	$s_2\,\mathcal{E}(q)$	b/s_2	-
H	$\mathcal{E}(q)$	b	-
D-E	$a\left(\mathcal{E}(\mu,q) - (1-q^2)\mathcal{F}(\mu,q)\right)$	s_2/a	b/s_2
E-F	$s_2\,\mathcal{E}(\mu,q)$	a/s_2	b/a
F	$\mathcal{E}(\mu,q)$	a	b/a
B-E	$b\left(\mathcal{E}(q) - (1-q^2)\mathcal{K}(q)\right)$	s_1/b	-
E-G	$s_1\,\mathcal{E}(q)$	b/s_1	-

$$\begin{aligned} I_\xi &= \frac{1}{\pi} \int_{a^2}^{1} \sqrt{\frac{t - s_2^2}{(t - a^2)(t - b^2)}}\, \mathrm{d}t \\ &= \frac{2}{\pi} \sqrt{a^2 - b^2} \Bigg((1 - q^2)\, \mathcal{F}(\mu, q) - \mathcal{E}(\mu, q) \\ &\qquad + \sqrt{\frac{1 - b^2}{a^2 - b^2}}\, \sin\mu \Bigg), \end{aligned} \quad (27)$$

where $\mathcal{F}(\mu, q)$ and $\mathcal{E}(\mu, q)$ are incomplete elliptic integrals of first and second kind, their amplitude μ given by $\sin^2\mu = (1 - a^2)/(1 - s_2^2)$. Approaching the point B with $s_2 \to a$ from below, we have $q \to 1$, $\mu \to \pi/2$, and $\mathcal{E}(\mu, q) \to \mathcal{E}(q) \to 1$, and therefore

$$\begin{aligned} I_\eta &\to \tfrac{2}{\pi} \sqrt{a^2 - b^2}, \\ I_\xi &\to \tfrac{2}{\pi} \left(\sqrt{1 - b^2} - \sqrt{a^2 - b^2} \right). \end{aligned} \quad (28)$$

The bifurcation at B (B− →B+) leaves the actions I_ζ and I_η unaffected but reduces I_ξ by a factor of 2; this is compensated by the multiplicity of tori changing from $m = 1$ to $m = 2$.

Tables 2 to 5 are a complete list of this kind of analytic results. They have been derived with help of

	$(\pi/2)I_\eta$	q	$\sin\mu$
A-B	$\sqrt{a^2-b^2}\left(\mathcal{E}(q)-(1-q^2)\mathcal{K}(q)\right)$	$\sqrt{\frac{s_2^2-b^2}{a^2-b^2}}$	-
B	$\sqrt{a^2-b^2}$	-	-
B-C	$\sqrt{s_2^2-b^2}\,\mathcal{E}(q)$	$\sqrt{\frac{a^2-b^2}{s_2^2-b^2}}$	-
C	$\sqrt{1-b^2}\,\mathcal{E}(q)$	$\sqrt{\frac{a^2-b^2}{1-b^2}}$	-
(D-E)−	$a\left(\mathcal{E}(q)-\mathcal{E}(\mu,q)-(1-q^2)(\mathcal{K}(q)-\mathcal{F}(\mu,q))\right)$	s_2/a	b/s_2
(D-E)+	$\frac{a}{2}\left(\mathcal{E}(q)-\mathcal{E}(\mu,q)-(1-q^2)(\mathcal{K}(q)-\mathcal{F}(\mu,q))\right)$	s_2/a	b/s_2
E-F	$s_2\left(\mathcal{E}(q)-\mathcal{E}(\mu,q)\right)$	a/s_2	b/a
F	$\mathcal{E}(q)-\mathcal{E}(\mu,q)$	a	b/a
B-E	$b\left((1-q^2)\mathcal{F}(\mu,q)-\mathcal{E}(\mu,q)\right)+a\sin\mu$	s_1/b	$\sqrt{\frac{a^2-b^2}{a^2-s_1^2}}$
(E-G)−	$\frac{1}{2}\left(a\sin\mu-s_1\,\mathcal{E}(\mu,q)\right)$	b/s_1	$\sqrt{\frac{a^2-s_1^2}{a^2-b^2}}$
(E-G)+	$a\sin\mu-s_1\,\mathcal{E}(\mu,q)$	b/s_1	$\sqrt{\frac{a^2-s_1^2}{a^2-b^2}}$

Table 4. Action integrals $\frac{\pi}{2}I_\eta$ for degenerate tori. I_η vanishes along the line A-D-G-H in the bifurcation diagram; it is hyperelliptic along the line C-F-H.

	$(\pi/2)I_\xi$	q	$\sin^2\mu$	c
A	$\sqrt{1-a^2}$	-	-	-
A-B	$\sqrt{a^2-b^2}\left((1-q^2)\mathcal{F}(\mu,q)-\mathcal{E}(\mu,q)+c\sin\mu\right)$	$\sqrt{\frac{s_2^2-b^2}{a^2-b^2}}$	$\frac{1-a^2}{1-s_2^2}$	$\sqrt{\frac{1-b^2}{a^2-b^2}}$
B−	$\sqrt{1-b^2}-\sqrt{a^2-b^2}$	-	-	-
B+	$\frac{1}{2}(\sqrt{1-b^2}-\sqrt{a^2-b^2})$	-	-	-
B-C	$\frac{1}{2}\sqrt{s_2^2-b^2}\,(c\sin\mu-\mathcal{E}(\mu,q))$	$\sqrt{\frac{a^2-b^2}{s_2^2-b^2}}$	$\frac{1-s_2^2}{1-a^2}$	$\sqrt{\frac{1-b^2}{s_2^2-b^2}}$
A-D	$a\left((1-q^2)\mathcal{F}(\mu,q)-\mathcal{E}(\mu,q)+c\sin\mu\right)$	s_1/a	$\frac{1-a^2}{1-s_1^2}$	$1/a$
D-G	$a\left((1-s_1^2/a^2)\mathcal{F}(\mu,q)-\mathcal{E}(\mu,q)+c\sin\mu\right)$	b/a	$\frac{1-a^2}{1-b^2}$	$1/a$
G-H	$\frac{s_2}{2}\,(c\sin\mu-\mathcal{E}(\mu,q))$	b/s_2	$\frac{1-s_2^2}{1-b^2}$	$1/s_2$
D-E	$a\left((1-q^2)(\mathcal{F}(\mu,q)-\mathcal{E}(\mu,q)+c\sin\mu)\right)$	s_2/a	$\frac{1-a^2}{1-s_2^2}$	$1/a$
E-F	$\frac{s_2}{2}\,(c\sin\mu-\mathcal{E}(\mu,q))$	a/s_2	$\frac{1-s_2^2}{1-a^2}$	$1/s_2$
(B-E)−	$b\left((1-q^2)\mathcal{F}(\mu,q)-\mathcal{E}(\mu,q)+c\sin\mu\right)-\frac{\pi}{2}I_\eta$	s_1/b	$\frac{1-b^2}{1-s_1^2}$	$1/b$
(B-E)+	$\frac{b}{2}\left((1-q^2)\mathcal{F}(\mu,q)-\mathcal{E}(\mu,q)+c\sin\mu\right)-\frac{\pi}{4}I_\eta$	s_1/b	$\frac{1-b^2}{1-s_1^2}$	$1/b$
(E-G)−	$s_1\,(c\sin\mu-\mathcal{E}(\mu,q))-\pi I_\eta$	b/s_1	$\frac{1-s_1^2}{1-b^2}$	$1/s_1$
(E-G)+	$\frac{s_1}{2}\,(c\sin\mu-\mathcal{E}(\mu,q))-\frac{\pi}{4}I_\eta$	b/s_1	$\frac{1-s_1^2}{1-b^2}$	$1/s_1$

Table 5. Action integrals $\frac{\pi}{2}I_\xi$ for degenerate tori. I_ξ vanishes along the line C-F-H in the bifurcation diagram.

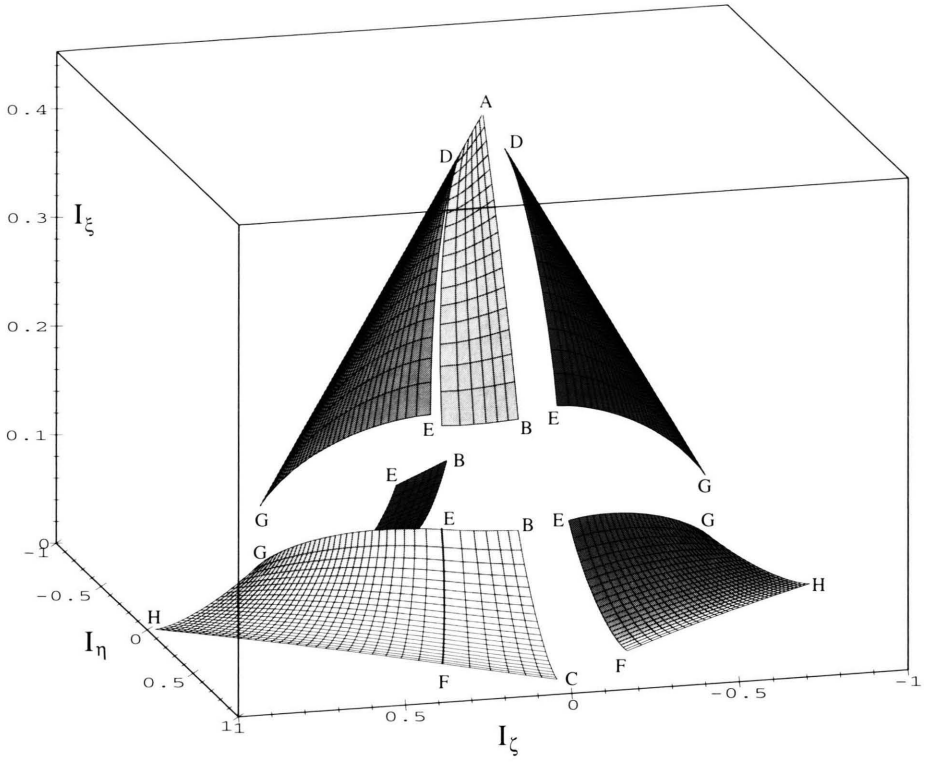

Fig. 9. Energy surface of billiard motion in the triaxial ellipsoid with parameters $(a, b) = (0.7, 0.3)$.

the tables in [15] and [16], and will serve as a backbone for the construction of energy surfaces, the "flesh" being filled in by numerical integration. The special Table 2 for point E of the bifurcation diagram determines how the energy surface is disrupted at this crossing of separatrix lines; the individual integrals are trivial, but there are four different limits.

Figure 9 shows the energy surface $H = E = \text{const}$ in the 3D-space of action variables I_ζ (right to left), I_η (back to front), and I_ξ (bottom to top). It may be viewed as a mapping of the bifurcation diagrams, Fig. 6, into action space; corresponding points are marked by the same letters A through H. The different types of motion are represented as distinct patches: one patch ABED for the purely oscillatory motion, and two patches each for the other three types of motion as they involve rotation. The two BCFE patches appear with different signs of I_η, η being the rotating coordinate; DEG and EFHG occur with the two signs of I_ζ. Altogether, this makes for seven patches, two of which match continuously along the line EF.

For comparison, Fig. 10 shows the corresponding energy surface for the symmetry reduced billiard, where the coordinates x, y, z are restricted to the positive octant, with elastic reflection at the planes $x = 0$, $y = 0$, $z = 0$. The surface is continuous (albeit with discontinuous slopes along the separatrices), and all actions are non-negative.

The action representation $H(I_\xi, I_\eta, I_\zeta) = E$ of phase space contains most of the relevant physics of a given system. There is a one-to-one correspondence between points on this surface and invariant Liouville-Arnol'd tori whose angular part is trivial: the angles θ_s conjugate to actions I_s change with constant angular frequency $\omega_s = \partial E / \partial I_s$. The only non-trivial part of their behavior, the values of ω_s, may also be obtained from the energy surface $H(I_\xi, I_\eta, I_\zeta) = E$, and will be computed in the subsequent section.

Interior points of a given patch represent 3-tori, boundary points correspond to critical tori or separatrices, i. e., they indicate bifurcations. The action values for boundaries have been assembled in Tables 2-5.

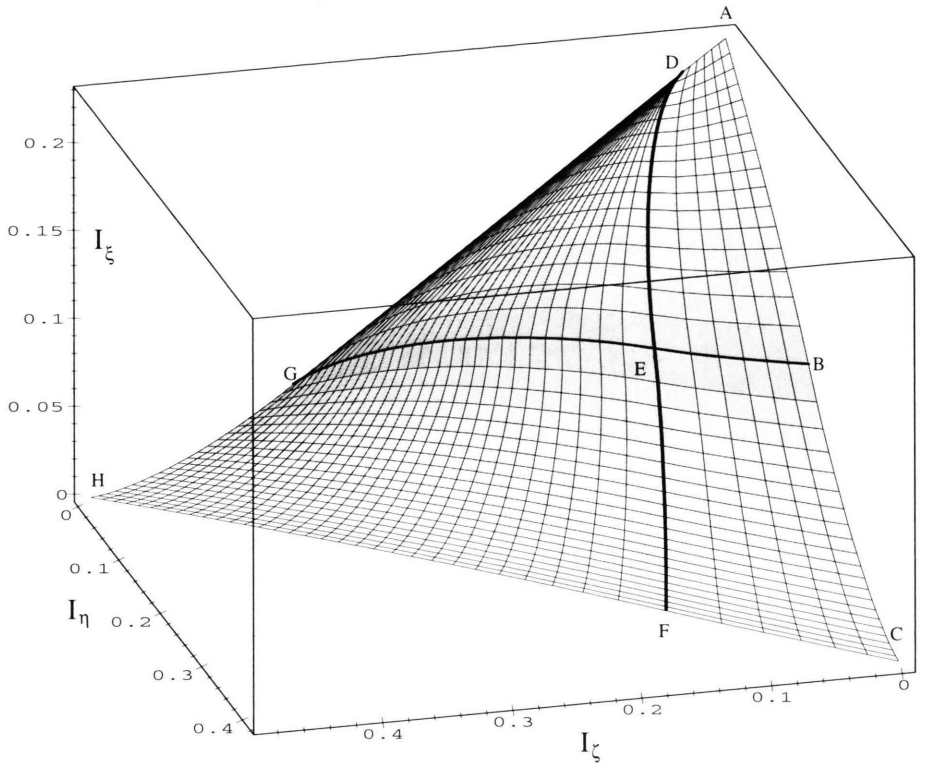

Fig. 10. Energy surface of billiard motion in the symmetry reduced triaxial ellipsoid with parameters $(a, b) = (0.7, 0.3)$.

In that sense these tables provide the skeleton of the energy surface.

Let us discuss the possible types of motion in terms of the properties of tori in the various patches, starting with critical cases. Compare Fig. 11 for orbits corresponding to the special points A through H. Point A represents a critical 1-torus, i. e., a single periodic orbit. We saw already that this is the (stable) oscillation along the ellipsoid's shortest axis. The edges A-B and B-C have $I_\zeta = 0$ and represent the (elliptic) 2-tori of planar billiard motion in the (y, z)-plane [7]. Tori along A-B are oscillatory motion that intersects the y-axis between the foci $(y, z) = (\pm\sqrt{a^2 - b^2}, 0)$; tori along B-C are rotational motion that surrounds these foci, turning into sliding motion along the ellipsoid's smallest circumference as point C is approached. The separatrix at B represents all (y, z)-planar motion that passes through the two foci, including the (unstable) linear oscillation along the y-axis.

The edges C-F and F-H have $I_\xi = 0$; they represent the (parabolic) 2-tori of geodesic motion on the ellipsoid's surface, C and H being elliptic-parabolic 1-tori

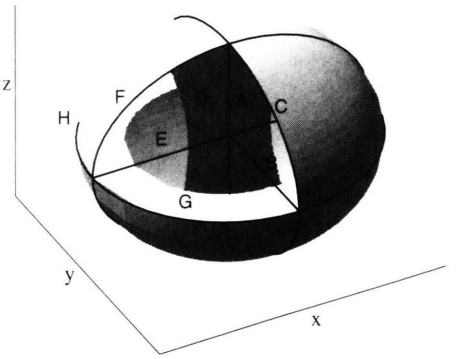

Fig. 11. Special orbits A through H for parameters $(a, b) = (0.7, 0.3)$. A, B, E are linear motion along the three principal axes. C, F, H are geodesic motion along the three principal circumferences. D is motion between the focal hyperbolas in the (x, z)-plane. G is motion outside the focal ellipse in the (x, y)-plane.

of periodic motion along the smallest ($x = 0$) and largest ($z = 0$) circumference, respectively. Point F corresponds to an hyperbolic-parabolic 1-torus (sliding along the middle circumference $y = 0$) which

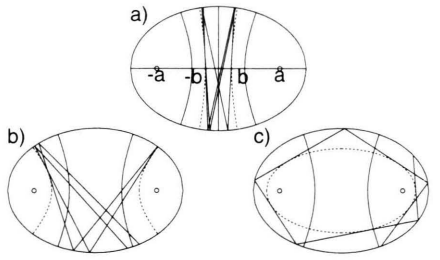

Fig. 12. Three kinds of planar billiard motion in the (x, z)-plane. a) Stable motion confined to the region between the focal hyperbolas, from segment A-D. b) Unstable motion that crosses the focal hyperbolas and intersects the x-axis between the foci at $x = \pm a$, from segment D-E. c) Unstable motion surrounding the foci, from segment E-F.

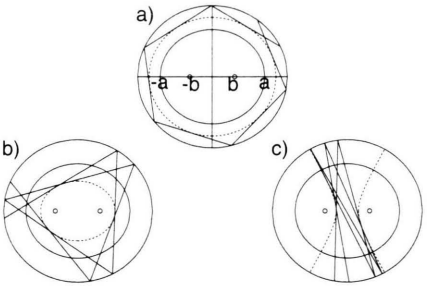

Fig. 13. Three kinds of planar billiard motion in the (x, y)-plane. a) Stable rotation outside the focal ellipse, from segment H-G. b) Unstable motion that crosses the focal ellipse and intersects the x-axis outside the foci at $x = \pm b$, from segment G-E. c) Unstable motion oscillating through the foci, from segment E-B.

separates geodesic motion with η-rotation about the x-axis (C-neighborhood) from geodesic motion with ζ-rotation about the z-axis (H-neighborhood).

There are three different planar elliptic billiards contained in the ellipsoidal dynamics. We saw that motion in the (y, z)-plane is found along the line A-B-C. Billiards in the (x, z)- and (x, y)-planes are represented by the lines A-D-E-F and H-G-E-B, respectively, each with three parts of different character: there are elliptic 2-tori along the segments A-D and H-G, and separatrices along the rest of the lines. This implies that the planar motion corresponding to the edges D-E-F and G-E-B results from a delicate combination of 3-tori in the limits $s_1 \to b\pm$ and $s_2 \to a\pm$.

Consider first the (x, z)-planar billiard, see Figure 12. Starting with the stable linear z- or ξ-oscillation at point A, the segment A-D contains (x, z)-motion bounded by the hyperbolas $\zeta = s_1 < b$. Physically this is a stable superposition of x- and z- (or ζ- and ξ-) oscillations. At point D, the motion is bounded by the focal hyperbolas $\zeta = b$. Between D and E, it intersects the x-axis between the foci $(x, z) = (\pm a, 0)$, and also cuts through the focal hyperbolas. The two parts $\eta = b$ and $\zeta = b$ of the (x, z)-plane (between and outside the focal hyperbolas, respectively) are then unstably embedded in a critical surface, with different limiting tori and actions as $s_1 \to b-$ and $s_1 \to b+$. At point E, the critical surface is even more complicated, involving the focal ellipse in addition to the focal hyperbolas. It contains the unstable linear oscillation along the x-axis which is composed of three kinds of pieces: the innermost piece $|x| < b$ has $(\xi, \eta) = (a, b)$; the two pieces $b < |x| < a$ have $(\xi, \zeta) = (a, b)$; the outer two parts $a < |x| < 1$ have $(\eta, \zeta) = (a, b)$. Hence the linear x-motion picks up actions I_ζ, I_η, and I_ξ, with multiplicities depending on the "corner" of E, cf. Table 2. The total action of this linear motion is of course simply $2/\pi$ which appears here as the sum of the three actions I_s at the corner $(s_1, s_2) = (b-, a-)$. Between E and F, the planar (x, z)-billiard surrounds the foci, and approaches the unstable geodesic motion along the $y = 0$ circumference.

The (x, y)-planar billiard is of similar complexity, see Figure 13. Starting at point H with the stable geodesic motion along the $z = 0$ circumference, the H-G edge comprises stable 2-tori corresponding to trajectories that stay outside the focal ellipse, $\xi \geq s_2 > a$, and never leave the region where $\eta = a$; hence $I_\eta = 0$. At point G, the focal ellipse becomes the inner envelope; then, along G-E, trajectories cross the focal ellipse, traversing regions where $\eta = a$ and regions where $\xi = a$; they still surround the foci $(x, y) = (\pm b, 0)$. The planar motion is embedded in a separatrix with different limits $s_2 \to a-$ and $s_2 \to a+$. The linear x-motion contained in the cross point E of separatrices has already been discussed. The segment E-B contains motion that intersects the x-axis between the foci, turning into linear oscillation along the y-axis as point B is approached.

We have discussed all boundaries of the patches ABED, BCFE, and FHGE. The motion type associated with interior points should thereby be clear; it is illustrated by the pictures of the corresponding caustics in Figure 8a, c, d. The last patch to be considered is DEG, with caustics as in Figure 8b. Its boundaries D-E and G-E are separatrices that have been discussed in connection with (x, z)- and (x, y)-planar motion,

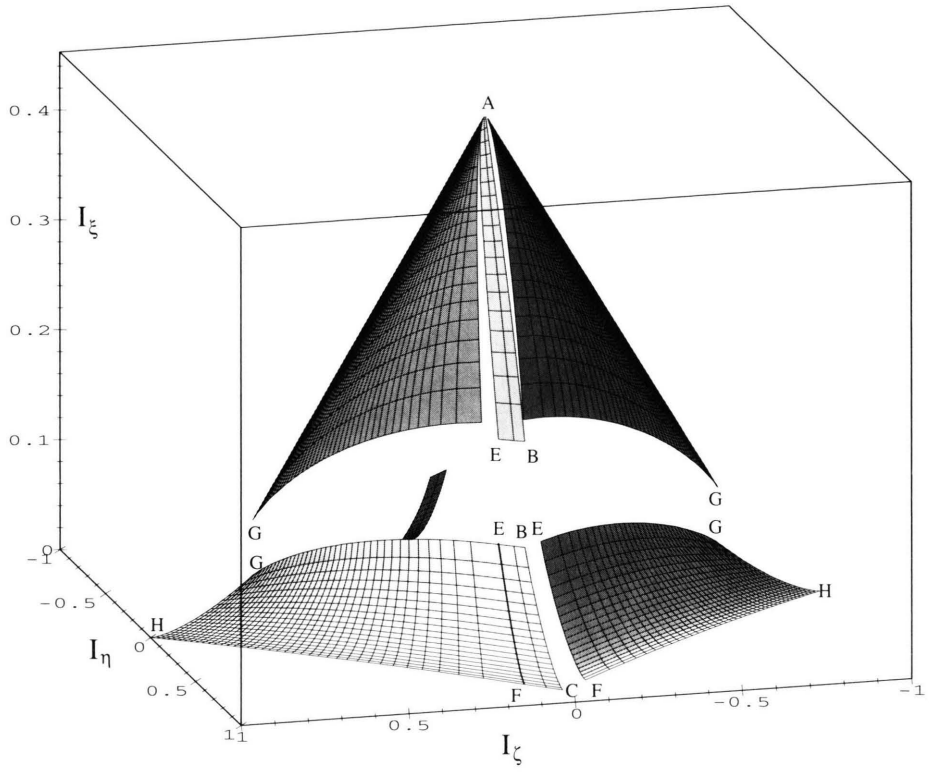

Fig. 14. Energy surface of an almost oblate ellipsoidal billiard; $(a, b) = (0.7, 0.1)$.

respectively. The boundary D-G is an interesting collection of elliptic 2-tori with $I_\eta = 0$; in configuration space these correspond to one-sheeted hyperboloids $\eta = \text{const}$, starting with the flat (x, z)-region between the focal hyperbolas at point D, and ending with the elliptic annulus outside the focal ellipse in the (x, y)-plane. We shall prove in the subsequent section, (59), that the edge D-G is a straight line, which means that all corresponding tori have the same winding number $W_{\zeta\xi} = \omega_\zeta/\omega_\xi$.

To end this section, we present energy surfaces for two different shapes of the ellipsoid. Figure 14 shows the case $(a, b) = (0.7, 0.1)$ which is close to the limit of oblate ellipsoids. The patches with $0 \leq s_1 \leq b$ have decreased in size whereas those with rotational ζ-motion dominate the picture. In the limit $b \to 0$, the variable ζ becomes the angle φ of rotation about the z-axis, and I_ζ the corresponding angular momentum L_φ. The corresponding energy surface has been given in [7].

Figure 15 shows the case $(a, b) = (0.51, 0.49)$ which is close to the limit of prolate ellipsoids. All patches except the two copies of BCFE have decreased; η-rotation about the x-axis becomes the dominating feature, and in the limit $b \to a$, η becomes the angle φ of rotation about the x-axis, I_η the corresponding angular momentum L_φ. Figure 15 should be compared to figure 8 in [7], which shows that point E develops into a special singularity at $(I_\xi, I_\eta, I_\zeta) \to ((1-a)/\pi, 0, 2a/\pi)$.

5. Frequencies and winding numbers

The angular frequencies $(\omega_\xi, \omega_\eta, \omega_\zeta)$ of rotation on the Liouville-Arnol'd tori are derived from the Hamiltonian in action variable representation, $H(I_\xi, I_\eta, I_\zeta) = E$, by means of the canonical equations

$$\omega_s = \frac{\partial H}{\partial I_s}. \tag{29}$$

In order to compute them from the actions as given in

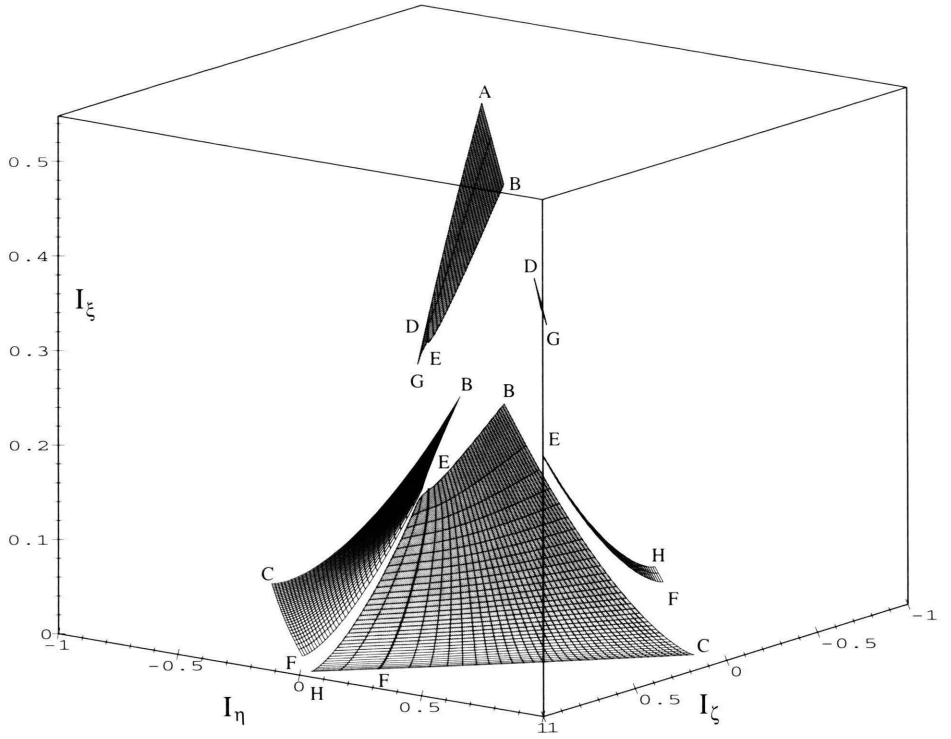

Fig. 15. Energy surface of an almost prolate ellipsoidal billiard; $(a, b) = (0.51, 0.49)$.

the previous section[4], $I_s = \sqrt{2E}\,\tilde{I}_s(s_1^2, s_2^2)$, we take the derivatives of H with respect to E, s_1^2, s_2^2 to obtain the three equations

$$\begin{pmatrix} 1 \\ 0 \\ 0 \end{pmatrix} = \begin{pmatrix} \tilde{I}_\xi & \tilde{I}_\eta & \tilde{I}_\zeta \\ I_{\xi,1} & I_{\eta,1} & I_{\zeta,1} \\ I_{\xi,2} & I_{\eta,2} & I_{\zeta,2} \end{pmatrix} \begin{pmatrix} \tilde{\omega}_\xi \\ \tilde{\omega}_\eta \\ \tilde{\omega}_\zeta \end{pmatrix}. \quad (30)$$

We have used the relations $\partial I_s/\partial E = \tilde{I}_s/\sqrt{2E}$ and the scaling $\tilde{\omega}_s = \omega_s/\sqrt{2E}$. The quantities $I_{s,1}$ and $I_{s,2}$ are

$$I_{s,1} = \frac{\partial \tilde{I}_s}{\partial s_1^2} \quad (31)$$

$$= \mp \frac{n_s}{4\pi} \int_{s_-}^{s_+} \sqrt{\frac{s^2 - s_2^2}{(s^2 - a^2)(s^2 - b^2)(s^2 - s_1^2)}}\, \mathrm{d}s,$$

$$I_{s,2} = \frac{\partial \tilde{I}_s}{\partial s_2^2} \quad (32)$$

$$= \mp \frac{n_s}{4\pi} \int_{s_-}^{s_+} \sqrt{\frac{s^2 - s_1^2}{(s^2 - a^2)(s^2 - b^2)(s^2 - s_2^2)}}\, \mathrm{d}s,$$

the sign depending on whether $s^2 - s_i^2$ is positive or negative in the interval of integration. This shows that even though the computation of frequencies, or periods $T_s = 2\pi/\omega_s$, is a little more involved than the computation of actions, knowledge of the latter is all that is needed. The integrals (31) and (32) are of the same category as the action integrals (22).

In order to avoid minor complications, and to have continuity of results even at separatrices, we consider here the symmetry reduced billiard, i. e., we take $n_\xi = n_\eta = n_\zeta = 2$, and multiplicities $m = 1$. It is not difficult to determine the appropriate factors of 2, wherever necessary, for the complete ellipsoid.

Figures 16-18 are plots of the time T_ξ and winding numbers $W_{\eta\xi} = \omega_\eta/\omega_\xi$ as well as $W_{\zeta\eta} = \omega_\zeta/\omega_\eta$,

[4]For the sake of this argument, ω_s and I_s are assumed unscaled by energy, whereas $\tilde{\omega}_s$ and $\tilde{I}_s$ are the scaled quantities. The tilde ˜ will be dropped again later on.

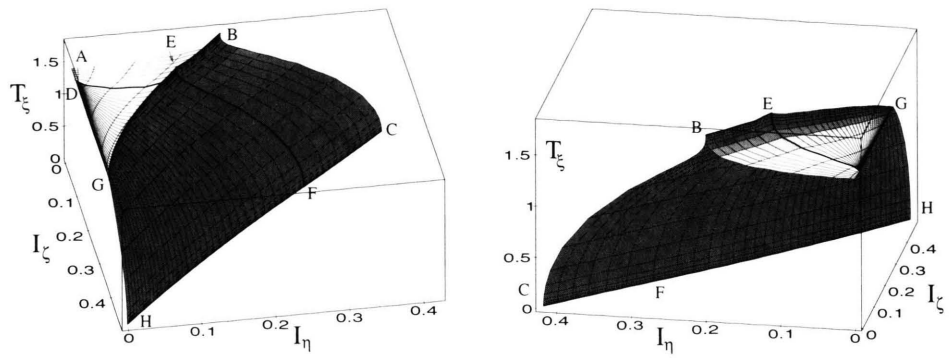

Fig. 16. Period $T_\xi = 2\pi/\omega_\xi$ plotted above the (I_η, I_ζ)-plane for the symmetry reduced ellipsoid with parameters $(a, b) = (0.7, 0.3)$.

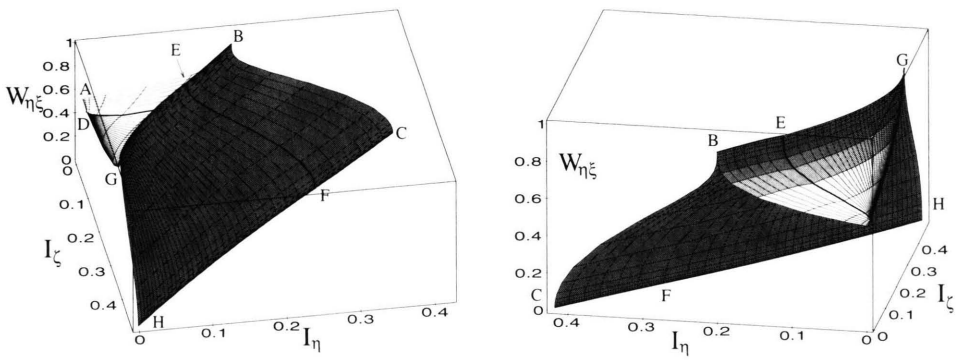

Fig. 17. Winding number $W_{\eta\xi} = \omega_\eta/\omega_\xi$ plotted above the (I_η, I_ζ)-plane for parameters $(a, b) = (0.7, 0.3)$.

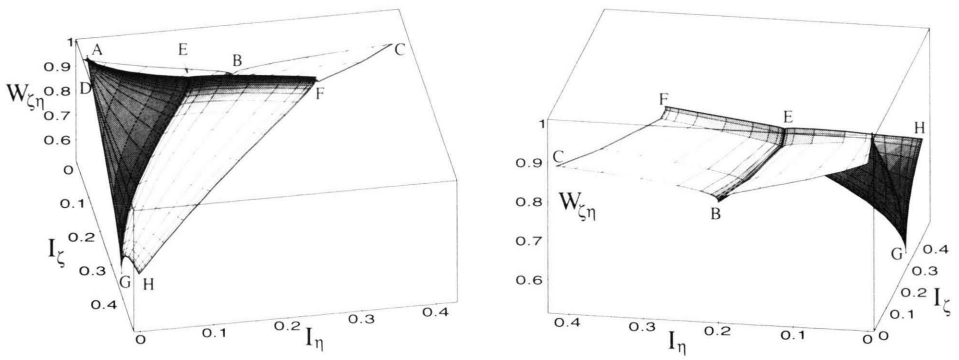

Fig. 18. Winding number $W_{\zeta\eta} = \omega_\zeta/\omega_\eta$ plotted above the (I_η, I_ζ)-plane for parameters $(a, b) = (0.7, 0.3)$.

above the (I_η, I_ζ)-plane of actions. Two different points of view are taken in each case, in order to support the three-dimensional impression. The graphs have been obtained by numerical integration, but boundaries and separatrices can be computed analytically. In the following we present explicit results for most of the interesting cases. The tilde ˜ will be dropped from now on; frequencies ω_s and actions I_s are assumed to be multiples of $\sqrt{2E}$.

Points A, C, and H are particularly simple. At A we have $I_\eta = I_\zeta = 0$ and $I_{\eta,1} = I_{\zeta,2} = 0$. The immediate consequence is

$$\omega_\xi = \frac{1}{I_\xi} = \frac{\pi}{\sqrt{1-a^2}}$$

or

$$T_\xi = \frac{2\pi}{\omega_\xi} = 2\sqrt{1-a^2}, \tag{33}$$

and for the other two frequencies

$$I_{\xi,2}\,\omega_\xi + I_{\eta,2}\,\omega_\eta = 0\,,\quad I_{\xi,1}\,\omega_\xi + I_{\zeta,1}\,\omega_\zeta = 0\,. \tag{34}$$

The four integrals $I_{s,i}$ are elementary,

$$\begin{aligned} I_{\xi,2} &= -\frac{1}{2\pi\sqrt{a^2-b^2}}\,\arcsin\sqrt{\frac{1-a^2}{1-b^2}} \\ I_{\eta,2} &= \frac{1}{4\sqrt{a^2-b^2}} \\ I_{\xi,1} &= -\frac{1}{2\pi a}\,\arccos a\,,\quad I_{\zeta,1} = \frac{1}{4a}\,. \end{aligned} \tag{35}$$

Consequently, the winding numbers $W_{\eta\xi} := \omega_\eta/\omega_\xi$ and $W_{\zeta\xi} := \omega_\zeta/\omega_\xi$, are given by

$$\sin\frac{\pi}{2}W_{\eta\xi} = \sqrt{\frac{1-a^2}{1-b^2}}\,,\quad \cos\frac{\pi}{2}W_{\zeta\xi} = a\,. \tag{36}$$

The results (33) and (36) are familiar from planar billiards, where they may be derived from the eigenvalues of a monodromy matrix, cf. [17]. The winding number $W_{\eta\xi}$ refers to oscillations along the z-axis, in the (y,z)-plane, with small amplitudes in y-direction, while $W_{\zeta\xi}$ describes oscillations in the (x,z)-plane.

Before we discuss the points C and H, we demonstrate that $T_\xi = 0$ along the line C-F-H, i. e., for geodesic flow. Physically, this is obvious, but formally it follows from inserting $I_\xi = I_{\xi,1} = 0$ into (30) which implies $\omega_\xi I_{\xi,2} = (I_{\eta,1}I_{\zeta,2} - I_{\zeta,1}I_{\eta,2})/(I_\eta I_{\zeta,1} - I_\zeta I_{\eta,1}) \neq 0$, and from

$$\begin{aligned} I_{\xi,2} &= -\frac{1}{2\pi}\sqrt{\frac{1-s_1^2}{(1-a^2)(1-b^2)}}\,\lim_{s_2\to 1}\int_{s_2}^{1}\frac{\mathrm{d}s}{\sqrt{s^2-s_2^2}} \\ &= 0\,. \end{aligned} \tag{37}$$

The approach $\to 0$ is proportional to $\sqrt{1-s_2}$, which is well borne out in Figure 16. Thus all along C-F-H we obtain ω_η and ω_ζ from

$$I_\eta\,\omega_\eta + I_\zeta\,\omega_\zeta = 1\,,\quad I_{\eta,1}\,\omega_\eta + I_{\zeta,1}\,\omega_\zeta = 0\,. \tag{38}$$

Now at point C we also have $I_\zeta = 0$, implying

$$\omega_\eta = \frac{1}{I_\eta} \text{ or } T_\eta = 2\sqrt{1-b^2}\,\mathcal{E}(q)\,, \tag{39}$$

with $q^2 = (a^2-b^2)/(1-b^2)$. As expected, T_η is half the length of the ellipsoid's smallest circumference. The frequency ω_ζ is obtained from (39) and

$$\begin{aligned} W_{\zeta\eta} = \frac{\omega_\zeta}{\omega_\eta} &= -\frac{I_{\eta,1}}{I_{\zeta,1}} \\ &= \frac{2}{\pi}\frac{ab}{\sqrt{1-b^2}}\left(\frac{1}{b^2}\,\Pi(\tfrac{\pi}{2}, 1-\tfrac{a^2}{b^2}, q) - \mathcal{K}(q)\right), \end{aligned} \tag{40}$$

where $\Pi(\frac{\pi}{2}, \alpha^2, q)$ is a complete elliptic integral of the third kind, with modulus q and parameter α^2. This follows from

$$I_{\zeta,1} = \frac{1}{2\pi}\,\frac{1}{ab}\,\lim_{s_1\to 0}\int_0^{s_1}\frac{\mathrm{d}s}{\sqrt{s_1^2-s^2}} = \frac{1}{4ab} \tag{41}$$

and

$$\begin{aligned} I_{\eta,1} &= -\frac{1}{2\pi}\int_b^a\sqrt{\frac{1-s^2}{(a^2-s^2)(b^2-s^2)}}\,\frac{\mathrm{d}s}{s} \\ &= -\frac{1}{2\pi}\frac{1}{\sqrt{1-b^2}}\left(\frac{1}{b^2}\,\Pi(\tfrac{\pi}{2}, 1-\tfrac{a^2}{b^2}, q) - \mathcal{K}(q)\right). \end{aligned} \tag{42}$$

Similarly, at point H we have $I_\eta = 0$, implying

$$\omega_\zeta = \frac{1}{I_\zeta} \text{ or } T_\zeta = 2\mathcal{E}(b)\,; \tag{43}$$

this is expected from the length of the ellipsoid's largest circumference. The frequency ω_η follows from (43) and

$$\begin{aligned} W_{\eta\zeta} = \frac{\omega_\eta}{\omega_\zeta} &= -\frac{I_{\zeta,1}}{I_{\eta,1}} \\ &= \frac{2a}{\pi}\,\frac{1-b^2}{\sqrt{(a^2-b^2)(1-a^2)}}\,\Pi\left(\tfrac{\pi}{2}, \alpha^2, b\right), \end{aligned} \tag{44}$$

where the parameter is $\alpha^2 = -b^2(1-a^2)/(a^2-b^2)$.

Consider now the line A-B-C where $I_\zeta = I_{\zeta,2} = 0$. Inversion of (30) leads to

$$\omega_\xi = \frac{I_{\eta,2}}{I_\xi\,I_{\eta,2} - I_\eta\,I_{\xi,2}} \tag{45}$$

and winding numbers

$$W_{\eta\xi} = -\frac{I_{\xi,2}}{I_{\eta,2}}, \quad W_{\zeta\eta} = \frac{I_{\xi,1} I_{\eta,2} - I_{\eta,1} I_{\xi,2}}{I_{\zeta,1} I_{\xi,2}}. \quad (46)$$

Evaluation of the various integrals along A-B gives

$$\omega_\xi = \frac{\pi}{\sqrt{a^2 - b^2}} \frac{1}{c \sin\mu - \mathcal{Z}(\mu, q)}, \quad (47)$$

where $\mathcal{Z}(\mu, q)$ is Jacobi's Zeta function,

$$\mathcal{K}(q)\mathcal{Z}(\mu, q) = \mathcal{K}(q)\mathcal{E}(\mu, q) - \mathcal{F}(\mu, q)\mathcal{E}(q), \quad (48)$$

and q, μ, c are given in Table 5. At point A, $s_2 \to b$, it is easy to recover (33), whereas at B, $s_2 \to a-$, we have the delicate limit $q \to 1$, $\mu \to \pi/2$, and

$$\begin{aligned} \omega_\xi &\approx \frac{\pi}{\sqrt{a^2 - b^2}} \frac{1}{c - \tanh \mathcal{F}(\mu, q)} \\ &\to \frac{\pi}{\sqrt{1 - b^2} - \sqrt{a^2 - b^2}}, \end{aligned} \quad (49)$$

with a logarithmic divergence in the derivative. Translated into time T_ξ, the result (49) gives the duration of two traversals, along the y-axis, from the ellipsoid's surface to the foci at $y = \sqrt{a^2 - b^2}$. The winding number $W_{\eta\xi}$ along A-B is

$$W_{\eta\xi} = \frac{\mathcal{F}(\mu, q)}{\mathcal{K}(q)}, \quad (50)$$

approaching $2\mu/\pi$ at point A, in agreement with (36), and 1 at point B.

The winding number $W_{\zeta\eta}$ involves more integrals and will not be derived here. The results along edge B-C are very similar and will also not be given explicitly.

The analysis is similar along the boundaries A-D and G-H of the energy surface. Between A and D we have $I_\eta = I_{\eta,1} = 0$, so (30) is solved by

$$\omega_\xi = \frac{I_{\zeta,1}}{I_\xi I_{\zeta,1} - I_\zeta I_{\xi,1}} \quad (51)$$

and winding numbers

$$W_{\eta\xi} = \frac{I_{\xi,1} I_{\zeta,2} - I_{\zeta,1} I_{\xi,2}}{I_{\zeta,1} I_{\eta,2}}, \quad W_{\zeta\xi} = -\frac{I_{\xi,1}}{I_{\zeta,1}}. \quad (52)$$

Between G and H we have $I_\eta = I_{\eta,2} = 0$, which leads to

$$\omega_\xi = \frac{I_{\zeta,2}}{I_\xi I_{\zeta,2} - I_\zeta I_{\xi,2}} \quad (53)$$

and winding numbers

$$W_{\eta\xi} = \frac{I_{\xi,2} I_{\zeta,1} - I_{\zeta,2} I_{\xi,1}}{I_{\zeta,2} I_{\eta,1}}, \quad W_{\zeta\xi} = -\frac{I_{\xi,2}}{I_{\zeta,2}}. \quad (54)$$

Instead of listing explicit expressions in terms of elliptic integrals, we refer to Figures 16-18.

Next we discuss the interesting edge D-G where $I_\eta = 0$ and $I_{\eta,1} + I_{\eta,2} = 0$. Solving (30) for the frequencies, we find

$$\omega_\xi = \frac{1}{I_\xi + I_\zeta W_{\zeta\xi}} \quad (55)$$

with winding numbers

$$\begin{aligned} W_{\eta\xi} &= \frac{I_{\xi,2} I_{\zeta,1} - I_{\zeta,2} I_{\xi,1}}{I_{\eta,1}(I_{\zeta,1} + I_{\zeta,2})}, \\ W_{\zeta\xi} &= -\frac{I_{\xi,1} + I_{\xi,2}}{I_{\zeta,1} + I_{\zeta,2}}. \end{aligned} \quad (56)$$

To compute $W_{\zeta\xi}$, observe that the factors $s^2 - s_1^2$ and $s^2 - s_2^2$ cancel in (31) and (32) if $s_1 = s_2$. We have

$$\begin{aligned} I_{\xi,1} &= I_{\xi,2} \\ &= -\frac{1}{2\pi} \int_a^1 \frac{\mathrm{d}s}{\sqrt{(s^2 - a^2)(s^2 - b^2)}} \\ &= -\frac{1}{2\pi a} \mathcal{F}(\mu, \tfrac{b}{a}) \end{aligned} \quad (57)$$

with $\sin^2\mu = (1 - a^2)/(1 - b^2)$, and similarly

$$I_{\zeta,1} = I_{\zeta,2} = \frac{1}{2\pi a} \mathcal{K}(\tfrac{b}{a}). \quad (58)$$

Hence,

$$W_{\zeta\xi} = \mathcal{F}(\mu, \tfrac{b}{a})/\mathcal{K}(\tfrac{b}{a}). \quad (59)$$

The frequency ω_ξ as given in (55) is evaluated with (59) and I_ξ, I_ζ from Tables 5 and 3:

$$\omega_\xi = \frac{\pi}{\sin\mu - a\mathcal{Z}(\mu, \frac{b}{a})}. \quad (60)$$

Like the winding ratio $W_{\zeta\xi}$, this is independent of s_1. We find the remarkable result that the one-sheeted confocal hyperboloids η = const are all generated from straight billiard trajectories of identical ω_ξ and ω_ζ.

With the general relationship

$$W_{\zeta\xi} = \frac{\omega_\zeta}{\omega_\xi} = -\left.\frac{\partial I_\xi}{\partial I_\zeta}\right|_{E,I_\eta} \tag{61}$$

between winding number and geometry of the energy surface, (59) is equivalent to the observation that the slope along D-G, in Figs. 9, 14, and 15, is constant for given (a, b).

Computation of the frequencies ω_η is more difficult. Direct application of (56) to the line D-G gives $W_{\eta\xi} = 0/0$, as

$$I_{\eta,1} = -\frac{1}{4}\frac{s_2 - s_1}{\sqrt{(a^2 - s_1^2)(s_1^2 - b^2)}} \to 0 \tag{62}$$

in the limit $s_2 \to s_1$. It is easy to see that the numerator of $W_{\eta\xi}$ in (56) is also of order $s_2 - s_1$, but the coefficients are elliptic integrals of the third kind, and there is not much to learn from the explicit expressions. We therefore leave it at that and refer to Fig. 17 which shows that ω_η increases considerably as point G is approached.

Let us finally consider the planar billiards along the edges D-E-F and B-E-G, starting with the segment D-E, i. e., motion in the (x, z)-plane that crosses the focal hyperbolas. The peculiarity here is that the integrals $I_{\eta,1}$ and $I_{\zeta,1}$ have logarithmic divergencies,

$$\begin{aligned} I_{\eta,1} &= -\frac{1}{2\pi}\int_b^{s_2}\sqrt{\frac{s_2^2 - s^2}{a^2 - s^2}}\,\frac{\mathrm{d}s}{s^2 - b^2}\,, \\ I_{\zeta,1} &= \frac{1}{2\pi}\int_0^{b}\sqrt{\frac{s_2^2 - s^2}{a^2 - s^2}}\,\frac{\mathrm{d}s}{b^2 - s^2}\,, \end{aligned} \tag{63}$$

but as the leading part of the singularity is the same in both integrals, we may extract it from the numerator and denominator of the inverse of (30), and obtain

$$\begin{pmatrix}\omega_\xi\\ \omega_\eta\\ \omega_\zeta\end{pmatrix} = \frac{1}{I_\xi(I_{\eta,2} + I_{\zeta,2}) - (I_\eta + I_\zeta)I_{\xi,2}}\begin{pmatrix} I_{\eta,2} + I_{\zeta,2}\\ -I_{\xi,2}\\ -I_{\xi,2}\end{pmatrix}. \tag{64}$$

Evaluation of the integrals is straightforward and leads to

$$\omega_\xi = \frac{\pi}{\sin\mu - a\mathcal{Z}(\mu, q)}\,, \tag{65}$$

$$\omega_\eta = \omega_\zeta = \pi\frac{\mathcal{F}(\mu, q)/\mathcal{K}(q)}{\sin\mu - a\mathcal{Z}(\mu, q)}\,. \tag{66}$$

Similar considerations along the edge E-F yield the same formal result, with a and s_2 interchanged, cf. Table 5. The fact that $W_{\zeta\eta} = \omega_\zeta/\omega_\eta = 1$ all along the line D-E-F is a prominent feature in Figure 18.

Analogous results hold along the line B-E-G, i. e., for motion in the (x, y)-plane that crosses the focal ellipse. The integrals $I_{\xi,2}$ and $I_{\eta,2}$ are divergent at $s = a$, and consideration of the leading terms results in

$$\begin{pmatrix}\omega_\xi\\ \omega_\eta\\ \omega_\zeta\end{pmatrix} = \frac{1}{I_\zeta(I_{\xi,1} + I_{\eta,1}) - (I_\xi + I_\eta)I_{\zeta,1}}\begin{pmatrix} -I_{\zeta,1}\\ -I_{\zeta,1}\\ I_{\xi,1} + I_{\eta,1}\end{pmatrix}. \tag{67}$$

Evaluation of the integrals gives

$$\omega_\xi = \omega_\eta = \frac{\pi}{\sin\mu - b\mathcal{Z}(\mu, q)}\,, \tag{68}$$

$$\omega_\zeta = \pi\frac{\mathcal{F}(\mu, q)/\mathcal{K}(q)}{\sin\mu - b\mathcal{Z}(\mu, q)} \tag{69}$$

for the segment B-E, and the same formulas, with b and s_1 interchanged, along E-G. The values of q and $\sin\mu$ are of course understood to be those listed in Table 5. The fact that $W_{\eta\xi} = \omega_\eta/\omega_\xi = 1$ all along the line B-E-G is well borne out in Figure 17.

Knowledge of the frequencies ω_ξ, ω_η, ω_ζ allows us to determine the location of resonances on the energy surface. This is relevant in connection with perturbations that spoil the integrability of the system, such as deformations of the ellipsoidal surface, or the addition of deflecting potentials. (Isotropic harmonic potentials are an interesting case of an integrable perturbation.) Perturbation theory breaks down at resonances, and chaotic motion tends to spread out from there, as well as from separatrices. A torus is called (n_ξ, n_η, n_ζ)-resonant if its frequencies obey the relation

$$n_\xi\omega_\xi + n_\eta\omega_\eta + n_\zeta\omega_\zeta = 0\,, \tag{70}$$

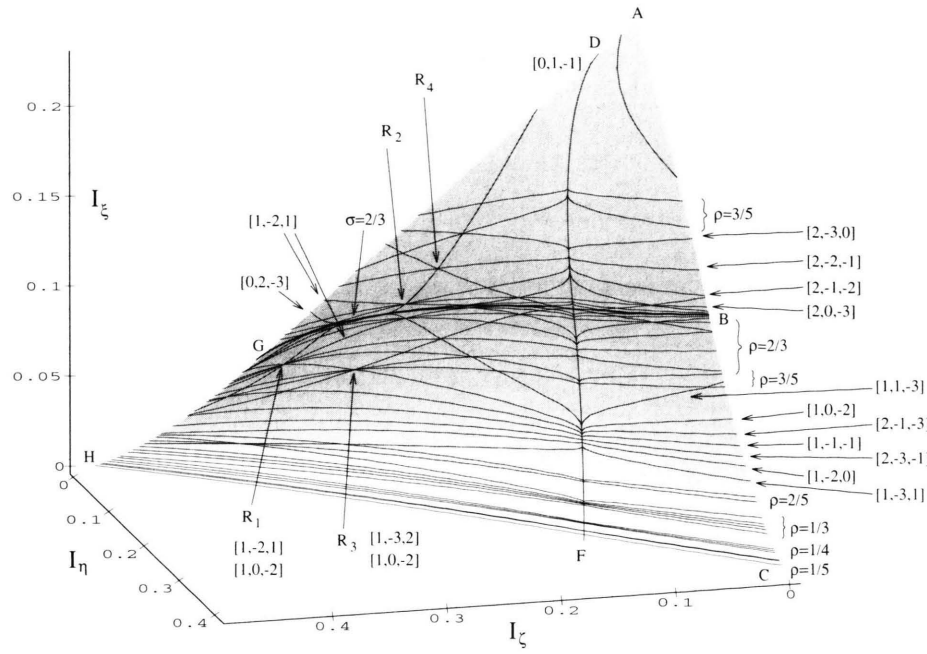

Fig. 19. Resonance lines on the energy surface of the symmetry reduced billiard with parameters $(a, b) = (0.7, 0.3)$, compare with Figure 10.

with integers n_ξ, n_η, n_ζ. The given 3-torus is then foliated by 2-tori. Equation (70) defines a line on the energy surface. The torus at an intersection of two resonance lines (n_ξ, n_η, n_ζ) and $(n'_\xi, n'_\eta, n'_\zeta)$ is foliated by periodic orbits whose periods are

$$\begin{aligned} T &= (n_\eta n'_\zeta - n_\zeta n'_\eta)\, T_\xi \\ &= (n_\zeta n'_\xi - n_\xi n'_\zeta)\, T_\eta \\ &= (n_\xi n'_\eta - n_\eta n'_\xi)\, T_\zeta \ . \end{aligned} \tag{71}$$

Lines defined by integer combinations of the sets (n_ξ, n_η, n_ζ) and $(n'_\xi, n'_\eta, n'_\zeta)$ pass through the same point, thus resonance lines tend to form networks with multiple intersections. Figure 19 shows the set of these lines with $|n_s| \leq 3$, for the symmetry reduced billiard $(a, b) = (0.7, 0.3)$.

Two lines of resonances have already been identified. We found in (66) that tori along D-E-F are $(0, 1, -1)$-resonant, and in (68) that tori along B-E-G are $(1, -1, 0)$-resonant. Some caution is in order, however, as these resonance lines are at the same time separatrices, i. e., *combinations* of tori, with different limiting tori on their two sides. Inspection of Fig. 19 shows that intersections of other resonance lines with these separatrices look different from ordinary intersections, such as points R_1-R_4.

From (59) we deduce that if $\mathcal{F}(\mu, \frac{b}{a})/\mathcal{K}(\frac{b}{a})$, with $\sin^2 \mu = (1 - a^2)/(1 - b^2)$, is a rational number m/n, then D-G is an $(m, 0, -n)$-resonance line.

In order to identify further resonances, we scan the separatrices for periodic orbits. Consider first the line segment E-F. Equations (65) and (66) tell us that resonance between ξ- and (η, ζ)-motion takes place if there are integers n_s such that

$$n_\xi\, \mathcal{K}(q) + (n_\eta + n_\zeta)\, \mathcal{F}(\mu, q) \ = \ 0 \ . \tag{72}$$

Now the allowed ratios

$$\rho \ := \ -\frac{n_\xi}{(n_\eta + n_\zeta)} \ =: \ \frac{n_\xi}{n_{\eta\zeta}} \tag{73}$$

range from 0 at F (where $\mu = 0$) to 1 at E (where $\mu = \frac{\pi}{2}$). They may be organized according to increasing values of denominators $n_{\eta\zeta}$, in the manner of a Farey tree (we choose n_ξ positive, so $n_{\eta\zeta}$ must also be positive). For given $n_{\eta\zeta}$, there is an infinite degeneracy in the possible choices of n_η and n_ζ, but this degeneracy is lifted as we leave the line E-F; the corresponding resonance lines spread out on the energy

surface. Let us concentrate on lines with the smallest possible n_ξ and $n_{\eta\zeta}$.

The case $\rho = 1/1$ is special in that it involves the singular point E. The $(1,-1,0)$-resonances E-B and E-G emanate from here, and we also have lines $(1,-2,1)$ and $(1,-3,2)$ in each of the four patches that join at E. But note that there are no $(1,n,-(n+1))$-resonance lines, $n \geq 0$, in the neighborhood of E; they are suppressed by the system of separatrices. The lines $(1,-2,1)$ start out very close to the separatrix B-E-G, and only gradually leave it. Two of them pass through the points R_1 and R_2; the other two cannot be distinguished from the line E-B in Figure 19. Similarly, two $(1,-3,2)$-resonances pass through R_3 and R_4 while the other two run to the neighborhood of B.

The most prominent resonance on E-F is $\rho = 1/2 = 2/4$. As the figure shows, it is the starting point of a bunch of seven resonance lines (with $|n_s| \leq 3$). These lines are initially tangent to E-F but soon spread sideways. One of them, the resonance $(1,0,-2)$, intersects the $\rho = 1$ lines discussed above in points R_1 and R_3. Another one, the resonance $(1,1,-3)$, first meets the separatrix E-G and then continues through points R_2 and R_4.

We have marked in Fig. 19 bunches $\rho = n_\xi/n_{\eta\zeta}$ with $n_{\eta\zeta}$ up to 5. As a general tendency, we observe that these bunches get narrower as we approach the line C-F-H of geodesic motion.

On the D-E part of the $(0,1,-1)$-resonance, the range of ρ-values depends on the parameters a and b, decreasing from 1 at E to $\rho_D = \mathcal{F}(\mu, \frac{b}{a})/\mathcal{K}(\frac{b}{a})$ at D. With our standard parameter choice $(a,b) = (0.7, 0.3)$, the value at D is 0.522, so we only see resonances $\rho = 2/3$ and $\rho = 3/5$.

Consider now the line segment B-E-G where (68) and (69) imply that ζ-motion is resonant with (ξ,η) if

$$(n_\xi + n_\eta)\,\mathcal{K}(q) + n_\zeta\,\mathcal{F}(\mu,q) \;=\; 0\,. \tag{74}$$

The situation is similar to that on D-E-F if instead of ρ and $n_{\eta\zeta}$ we introduce

$$\sigma \;:=\; -\frac{(n_\xi + n_\eta)}{n_\zeta} \;=:\; \frac{n_{\xi\eta}}{n_\zeta}\,. \tag{75}$$

The range of possible σ-values, however, is narrower than that of ρ. Along E-G, σ decreases from 1 to $\sigma_G = \rho_D \approx 0.522$, whereas between E and B it decreases from 1 to $2\mu/\pi \approx 0.806$. Hence there are no low order resonances on the segment B-E, and the only conspicuous resonance on E-G is $\sigma = 2/3$, with lines

$(2,0,-3)$, crossing over to the $\rho = 2/3$ resonances on D-E-F;

$(1,1,-3)$, one of them crossing to the $\rho = 1/2$ resonance on E-F, the other moving up through points R_2 and R_4, ending on the edge D-G;

$(0,2,-3)$, one moving down through point R_1, the other terminating on D-G.

The overall picture that we obtain from Fig. 19 is that the scheme of resonances is organized by the separatrices D-E-F and B-E-G. Most low order periodic orbits lie on these lines, i. e., they are of the planar billiard motion type. There are but a few notable exceptions, like point R_1 where $\omega_\xi = 2\omega_\zeta$, and $\omega_\xi + \omega_\zeta = 2\omega_\eta$; this corresponds to periodic 3D-motion with $4T_\xi = 3T_\eta = 2T_\zeta$.

As another example with an interesting scheme of resonances, Fig. 20 presents the case of the symmetry reduced prolate ellipsoid $a = b = 0.7$. Its relation to the general ellipsoid has been discussed in connection with Fig. 15; the patch B-C-F-E is all that survives the limit $b \to a$. Both resonance lines $(1,-1,0)$ (B-E) and $(0,1,-1)$ (E-F) lie in the plane $I_\eta = 0$, and join in the singular point E. Line E-F may be parametrized by values ρ as in (73), ranging from 0 at F to 1 at E. The corresponding parameter on line E-B is σ as in (75), ranging from 1 at E to 0.506 at B.

The figure shows the network of resonance lines with $n_s \leq 3$. There is a tendency of these lines to swing around point E, from segment E-F to segment E-B, their intersections producing a regular scheme of periodic orbits. We mention three infinite families with accumulation point E. The $(1,-2,1)$-resonance line starting in E intersects the $\rho = 1/2$ lines $(1,n,-n-2)$, and also the $\sigma = 2/3$ lines $(n,2-n,-3)$, in a sequence of periodic orbits with periods

$$\begin{aligned} T_n &= (n+4)T_\xi = (n+3)T_\eta = (n+2)T_\zeta, \\ &\qquad (n = 0,1,\ldots)\,; \end{aligned} \tag{76}$$

the first of these points, with $n = 0$, is marked as R_1 in Figure 20. The intersections of the $(1,-3,2)$-resonance with the $\rho = 1/2$ lines $(1,n,-n-2)$ are periodic orbits with periods

$$\begin{aligned} T_n &= (n+6)T_\xi = (n+4)T_\eta = (n+3)T_\zeta, \\ &\qquad (n = 0,1,\ldots)\,, \end{aligned} \tag{77}$$

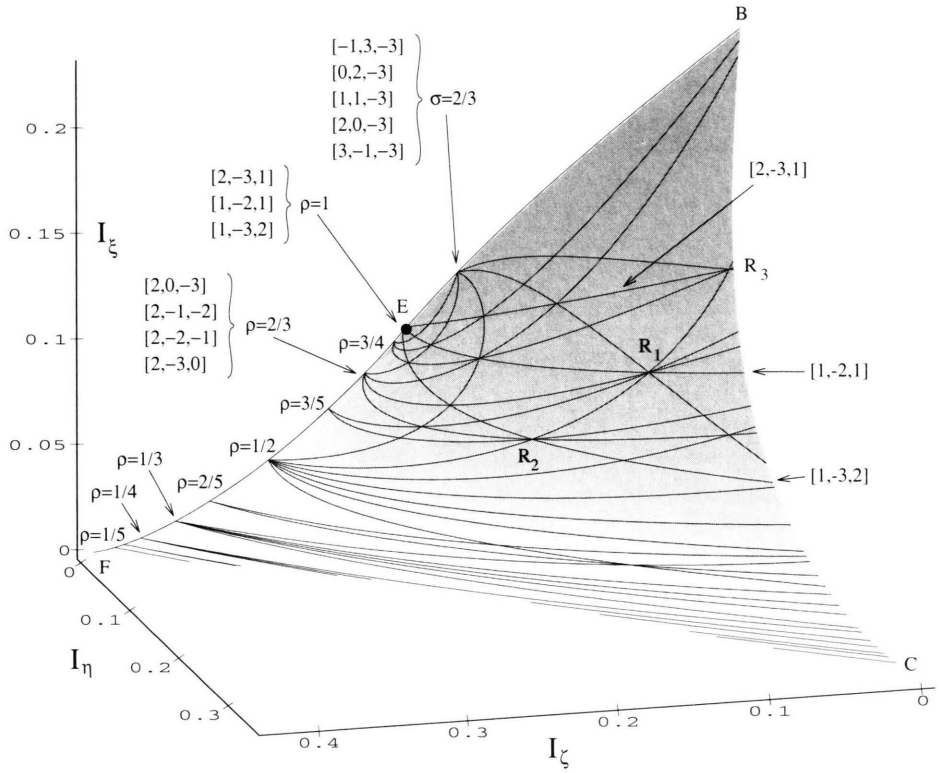

Fig. 20. Resonance lines on the energy surface of the symmetry reduced billiard with parameters $(a, b) = (0.7, 0.7)$.

the first one being marked as R_2. The third family is generated by intersections of the $(2, -3, 1)$-resonance with the $\rho = 1/2$ lines $(1, n, -n - 2)$:

$$T_n = (2n + 6)T_\xi = (2n + 5)T_\eta = (2n + 3)T_\zeta, \quad (n = 0, 1, \ldots), \tag{78}$$

R_3 being the first in this sequence.

As $a = b \to 0$, the prolate ellipsoid degenerates into a sphere. On the corresponding energy surface, point E moves up towards B and vanishes there; I_ξ depends only on the sum $I_\eta + I_\zeta$ (which is the total angular momentum, see [7]). The degeneracy of resonance lines with $\rho = \text{const}$ is then not lifted, but continues all across the surface from the plane $I_\eta = 0$ to $I_\zeta = 0$.

Acknowledgements

We are indebted to Holger Dullin for many enlightening discussions, and for his support in numerical computations. We benefitted from the work that he and Andreas Wittek had invested in the computer laboratory of our group. Much of the graphical work was done with the help of MAPLE.

[1] C. G. J. Jacobi, Vorlesungen über Dynamik. Chelsea Publ., New York 1969.
[2] M. V. Berry, Regular and irregular motion. In S. Jorna, editor, Topics in Nonlinear Dynamics, Vol. No. 46 of AIP Conference Proceedings, pages 16 - 120. American Institute of Physics, New York 1978.
[3] M. V. Berry, Eur. J. Phys. **2**, 91 (1981).
[4] M. C. Gutzwiller, Chaos in Classical and Quantum Mechanics, Vol. 1 of Interdisciplinary Applied Mathematics. Springer, Berlin 1990.
[5] Richter, P. H., Die Theorie des Kreisels in Bildern; Report 226, Institut für Dynamische Systeme, Universität Bremen, Bremen 1990.
[6] H. R. Dullin, M. Juhnke, and P. H. Richter, Bifurcation and Chaos **4**, 1535 (1994).
[7] P. H. Richter, A. Wittek, M. P. Kharlamov, and A. P. Kharlamov, Z. Naturforsch. **50a**, 693 (1995).
[8] P. M. Morse and H. Feshbach, Methods of Theoretical Physics. McGraw-Hill, New York 1953.
[9] L. D. Landau E. M. and Lifshitz, Mechanics. Pergamon Press, Oxford, New York 1984.
[10] S. Chang and R. Friedberg, J. Math. Phys. **29**, 1537 (1988).
[11] V. I. Arnold, Mathematical Methods of Classical Mechanics, Vol. 60 of Graduate Texts in Mathematics. Springer, Berlin 1978.
[12] K. Schwarzschild, Gesammelte Werke, Ed. H. H. Voigt. Springer, Berlin 1992.
[13] K. Schwarzschild, Zur Quantenhypothese. Sitz. Ber. Kgl. Preuss. Akad. d. Wiss. Berlin 1916: 548 - 568, 1916.
[14] William H. Press, Brian P. Flannery, Saul A. Teukolsky, and William T. Vetterling, Numerical Recipes in C. The Art of Scientific Computing, Cambridge University Press, Cambridge 1988.
[15] I. S. Gradshteyn and I. M. Ryzhik, Tables of Integrals, Series, and Products, Academic Press, New York 1965.
[16] Paul F. Byrd, and Morris D. Friedman, Handbook of Elliptic Integrals for Engineers and Physicists. Springer, Berlin 1971.
[17] H. R. Dullin, P. H. Richter, and A. Wittek, Chaos **6**, 43 (1996).